Tracking fluid mixing in epithermal deposits – Insights from in-situ $\delta^{18}O$ and trace element composition of hydrothermal quartz from the giant Cerro de Pasco polymetallic deposit, Peru

Rottier, Bertrand; Kouzmanov, Kalin; Casanova, Vincent; Bouvier, Anne-Sophie; Baumgartner, Lukas P.; Wälle, Markus; Fontboté, Lluís

How to cite

ROTTIER, Bertrand et al. Tracking fluid mixing in epithermal deposits – Insights from in-situ $\delta^{18}O$ and trace element composition of hydrothermal quartz from the giant Cerro de Pasco polymetallic deposit, Peru. In: Chemical Geology, 2021, vol. 576, n° 120277. doi: 10.1016/j.chemgeo.2021.120277

This publication URL: https://archive-ouverte.unige.ch/unige:151384
Publication DOI: 10.1016/j.chemgeo.2021.120277

Chemical Geology 576 (2021) 120277

Contents lists available at ScienceDirect

Chemical Geology

journal homepage: www.elsevier.com/locate/chemgeo

Tracking fluid mixing in epithermal deposits – Insights from in-situ $\delta^{18}O$ and trace element composition of hydrothermal quartz from the giant Cerro de Pasco polymetallic deposit, Peru

Bertrand Rottier [a,b,c,*], Kalin Kouzmanov [c], Vincent Casanova [c], Anne-Sophie Bouvier [d], Lukas P. Baumgartner [d], Markus Wälle [e,1], Lluís Fontboté [c]

[a] Département de Géologie et Génie Géologique, Université Laval, Québec, Canada
[b] Centre de Recherche Sur la Géologie et l'ingénierie des Ressources Minérales (E4m), Québec, Canada
[c] Department of Earth Sciences, University of Geneva, 1205 Geneva, Switzerland
[d] Institute of Mineralogy and Geochemistry, University of Lausanne, 1015 Lausanne, Switzerland
[e] Institute of Geochemistry and Petrology, ETH Zürich, 8092 Zürich, Switzerland

ARTICLE INFO

Editor: Dr. Christian France-Lanord

Keywords:
Oxygen isotope
SIMS
Quartz
Trace element
Epithermal deposit
Porphyry system

ABSTRACT

Ore precipitation in mineral deposits formed in the upper parts of a porphyry system, at shallow crustal level (< 1.5 km), such as epithermal Au-Ag-(Cu)-(As) and polymetallic deposits is often triggered by fluid cooling and/or mixing between fluids from different sources. Commonly, in such deposits, two main fluid sources are identified a deeply sourced magmatic fluid and a shallow meteoric water stored in a surficial aquifer. Oxygen and hydrogen isotope compositions of gangue and alteration minerals using conventional bulk isotopic methods support the existence of mixing between these two fluid types. However, bulk isotope analysis provides only limited information on the exact mixing mechanisms and on the changing proportions of the involved fluids. Due to their high spatial resolution, SIMS in-situ oxygen isotope and LA-ICP-MS trace element analyses, in transects across growth zones of single crystals are adequate tools to trace the dynamics of this fluid mixing. In this study, in-situ SIMS oxygen isotope and LA-ICP-MS trace element analyses were performed on 10 selected quartz crystals from the giant Cerro de Pasco porphyry-related epithermal polymetallic deposit in central Peru. The results, combined with previous microthermometric and LA-ICP-MS fluid inclusion studies on the same or equivalent crystals, allow quantifying and documenting the mixing between different types of fluids that formed the large Cerro de Pasco epithermal polymetallic deposit. The $\delta^{18}O_{quartz}$ values range between 4‰ and 20‰ and display variations up to 11.5‰ inside single crystals that cannot be only, nor mainly ascribed to fluid temperature changes. Rather, these variations record variable mixing proportions of a rising moderate-salinity magmatic fluid with a $\delta^{18}O_{H2O}$ around 10‰ and a low-salinity fluid with a $\delta^{18}O_{H2O}$ between 0 and 4‰, the latter stored below the paleo-water table. Each analyzed quartz crystals also display important variation of their trace element content, with Al (43 to 2098 ppm), Li (0.7 to 18 ppm), Ge (1.1 to 24ppm) and Ti (0.8 to 10 ppm). These variations do not systematically correlate with oxygen isotope compositions. This suggests that quartz trace element content is controlled by a complex interplay of fluid composition, temperature, pressure, and growth rate. Application of published Ti-in-quartz geothermometers on quartz grains from which the precipitation temperature is well constrained by fluid inclusion microthermometry, shows that it can lead to overestimation or underestimation of precipitation temperatures by more than 50 °C.

The obtained $\delta^{18}O_{quartz}$ patterns measured along profiles in the studied quartz crystals, and less clearly the in-situ trace element compositions, reveal abrupt changes and suggest that mixing between magmatic and surface-derived low-salinity fluids was not a continuous process. It rather took place through the influx of multiple short-lived pulses of magmatic fluid into the surface-derived low-salinity fluid surface aquifer.

* Corresponding author at: Département de Géologie et Génie Géologique, Université Laval, Québec, Canada
E-mail address: bertrand.rottier@ggl.ulaval.ca (B. Rottier).
[1] Present address: Memorial University of Newfoundland, CREAIT, CRC and CFI Services (CCCS), Bruneau Centre for Research and Innovation, St. John's, NL, Canada, A1C 5S7.

https://doi.org/10.1016/j.chemgeo.2021.120277
Received 25 January 2021; Received in revised form 5 April 2021; Accepted 21 April 2021
Available online 24 April 2021

1. Introduction

Mixing between rising magmatic fluids and cooler surficial meteoric water is a common mechanism in the upper part of porphyry systems. Such mixing is often invoked for the formation of high- and low-sulfidation Au-Ag-(Cu)-(As) epithermal deposits (Sillitoe, 1973; Dilles, 1987; Eastoe, 1978; Henley and McNabb, 1978; Sun and Eadington, 1987; Hedenquist and Lowenstern, 1994; Arribas, 1995), and also of porphyry-related epithermal polymetallic deposits (i.e., Cordilleran polymetallic deposits; Rye and Sawkins, 1974; Norman and Landis, 1983; Bussell et al., 1990; Deen et al., 1994; Beuchat et al., 2004; Field et al., 2005; Baumgartner et al., 2008; Catchpole et al., 2015; Rottier et al., 2018a). So far, fluid mixing in mineralized epithermal systems was mainly studied using bulk stable O and/or H isotope composition of hydrothermal minerals often combined with fluid inclusion studies (e.g., Beuchat et al., 2004; Wallier et al., 2006; Catchpole et al., 2015). However, hydrothermal minerals are commonly chemically zoned reflecting changing physicochemical conditions during their growth (Allan and Yardley, 2007; Rusk et al., 2008; Rottier et al., 2018a). Therefore, bulk stable isotope analyses performed on mineral separates, reflecting a partially averaged isotopic signature of the mineralized fluids, provide only limited information on the history of the mixing events (Allan and Yardley, 2007; Jourdan et al., 2009a; Tanner et al., 2013). On the contrary, few previous in-situ SIMS oxygen isotope studies performed on quartz from porphyry-related epithermal precious metal deposits have revealed strong variations of $\delta^{18}O_{quartz}$ values in single quartz crystals suggesting complex fluid mixing dynamics (Allan and Yardley, 2007; Tanner et al., 2013).

The focus of this contribution is the giant Cerro de Pasco epithermal polymetallic (Zn-Pb-Ag-Cu-Bi) deposit in Peru, emplaced at shallow level, its upper part being no more than 500 m below the paleo-surface, and at the border of a Miocene diatreme-dome complex. Thanks to previous studies (Einaudi, 1977; Baumgartner et al., 2008; Baumgartner et al., 2009; Rottier et al., 2016a; Rottier et al., 2018a) hydrothermal processes at the origin of this giant deposit are well characterized, and it has been shown that the main ore-forming processes are mixing of moderate- and low-salinity fluids. The here presented high-spatial resolution in-situ SIMS oxygen isotope analyses performed on successive growth zones of 10 selected quartz grains, on which SEM-CL images and trace element composition (LA-ICP-MS) were also acquired, allow to reconstruct with much more details the mixing history between these distinct fluids.

2. Geological setting and mineralization

Cerro de Pasco is one of the largest known porphyry-related epithermal polymetallic ("Cordilleran") deposits; it is located ~150 km North-East of Lima in the Western Cordillera of Peru, at an elevation of 4300 m.a.s.l. (Fig. 1A). It is part of the mid-Miocene metallogenic belt of central and northern Peru (Noble and McKee, 1999; Bissig et al., 2008; Bendezú and Fontboté, 2009; Bissig and Tosdal, 2009). Historical production and remaining resources aggregate more than 200 million tons (Mt) at approximately 7 wt% Zn, 2 wt% Pb, and 3 oz./t Ag in addition to at least 100 Mt. at 1.3% Cu and 1 g/t Au (Baumgartner et al., 2008; Rottier et al., 2018a). Furthermore, Cerro de Pasco produced more than 1 billion ounces of Ag during colonial times (Baumgartner et al., 2008 and references therein). The Cerro de Pasco district mainly consists of a large diatreme-dome complex of 2.5 km in diameter, emplaced west of a major high-angle N15°W-striking reverse fault, locally named the Longitudinal fault (Fig. 1B). The diatreme-dome complex intrudes weakly metamorphosed black shale and phyllites of the Devonian Excelsior Group (Saintilan et al., 2021) and polymictic conglomerates and sandstones of the Middle-Late Triassic Mitu Group (Spikings et al., 2016; Fig. 1B). East of the Longitudinal fault a thick sequence (about 1000 m) of massive carbonate rocks, mainly limestone with locally sandy intercalation, black bituminous limestone, and beds with chert nodules, belonging to the Late Triassic Chambará Formation (Pucará Group, Rosas et al., 2007), is exposed (Angeles, 1999).

The diatreme-dome complex was formed by a succession of phreatomagmatic, magmatic, and phreatic events spanning from 15.36 ± 0.03 Ma to 15.16 ± 0.04 Ma (zircon U-Pb ID-TIMS; Fig. 1; Einaudi, 1968 and 1977; Baumgartner et al., 2009; Rottier et al., 2020). An early phase of explosive activity produced a large diatreme-breccia more than 1.3 km-deep and 2 km-wide (Fig. 1B; Rottier et al., 2018b). The diatreme breccia was then intruded by a series of dacitic to rhyodacitic volcanic and subvolcanic bodies and by up to 20 m large east-west trending quartz-monzonite porphyry dykes (Fig. 1B). In the district, three temporally distinct events of porphyry-type mineralization were identified (PM1, PM2, and PM3); they are minor in terms of mineralized volume of rocks (Rottier et al., 2016b; Rottier et al., 2018b). They were formed slightly before and during the different dated phases of magmatic activity (Rottier et al., 2016b, 2018b; Rottier et al., 2020). Extensive pervasive pyrophyllite-quartz-pyrite alteration grading to illite-smectite-muscovite-pyrite and more externally to chlorite-calcite-pyrite alteration affects the central and the northern part of the diatreme-dome complex (Fig. 1B). This alteration is interpreted to have developed close to the surface by acidic magmatic vapors, generated by degassing of the deep part of the porphyry system and predating the epithermal polymetallic mineralization (Rottier et al., 2018a, 2018b, 2020).

The epithermal polymetallic mineralization occurs along the eastern margin of the diatreme-dome complex, mainly replacing rocks of the Pucará carbonate sequence (Fig. 1B; Einaudi, 1977; Baumgartner et al., 2008; Rottier et al., 2016a and 2018a). This mineralization was formed at a shallow level, its upper part <500 m below the paleo-surface, based on field relationships and textural characteristics of pyroclastic rocks (e.g., occurrence of lapilli tuff; Baumgartner, 2007, Baumgartner et al., 2008). It consists of three successive main mineralization stages resulting in a general transition from low- to high-sulfidation mineral assemblages. Detailed petrographic description of the different mineralization stages can be found in Einaudi (1977), Baumgartner et al. (2008), Rottier et al. (2016a) and Rottier et al., (2018a), and only the main characteristics are summarized here. The first mineralization stage (A), nomenclature and sequence according to Rottier et al. (2016a) and Rottier et al., (2018a), consists of several pipe-like pyrrhotite-dominated carbonate replacement bodies grading outwards into Fe-rich sphalerite (up to 80 vol%) and galena. These pipes are structurally controlled and replace the Pucará carbonates along the NNW-SSE Longitudinal fault corridor, and subordinately along N 35° and N 120° secondary faults (Einaudi, 1977; Baumgartner et al., 2008; Rottier et al., 2016a). The second epithermal polymetallic stage (B) comprises two sub-stages B_1 and B_2. Stage B_1 consists of a set of quartz-pyrite veins with minor amount of chalcopyrite, hematite, magnetite, light-brown sphalerite, galena, and tetrahedrite-tennantite. These veins are spatially associated with kaolinite-sericite-pyrite or sericite-pyrite alterations affecting the diatreme-dome complex. Stage B_2 consists of a massive pyrite-quartz body composed of ~90 vol% of pyrite and ~10 vol% of quartz. It is ~1.5 km in length, 250 m-wide and more than 550 m-deep. It is emplaced along the contact between the carbonate rocks and the diatreme-dome complex, and it replaces mainly Pucará carbonate rocks and only locally the diatreme breccia (Fig. 1B). The pyrite-quartz body shows a sericite-pyrite alteration halo up to 50 m-wide affecting the diatreme-dome complex (Einaudi, 1968; Baumgartner et al., 2008). No crosscutting relationships between the two sub-stages have been observed. During the last mineralization stage (C) two distinct types of orebodies, considered synchronous, were formed: high- to intermediate-sulfidation Zn-Pb-(Bi-Ag-Cu) carbonate replacement orebodies (stage C_1) and a set of *E*-W trending Cu-Ag-(Au-Zn-Pb) enargite-pyrite veins hosted in the diatreme-dome complex (stage C_2). The Zn-Pb-(Bi-Ag-Cu) orebodies (stage C_1), replace Pucará carbonate rocks in the eastern part of the deposit. They form large irregular upward-flaring 50 cm to around 50 m-wide and up to 400 m-long pipe-like bodies, mainly following N60-

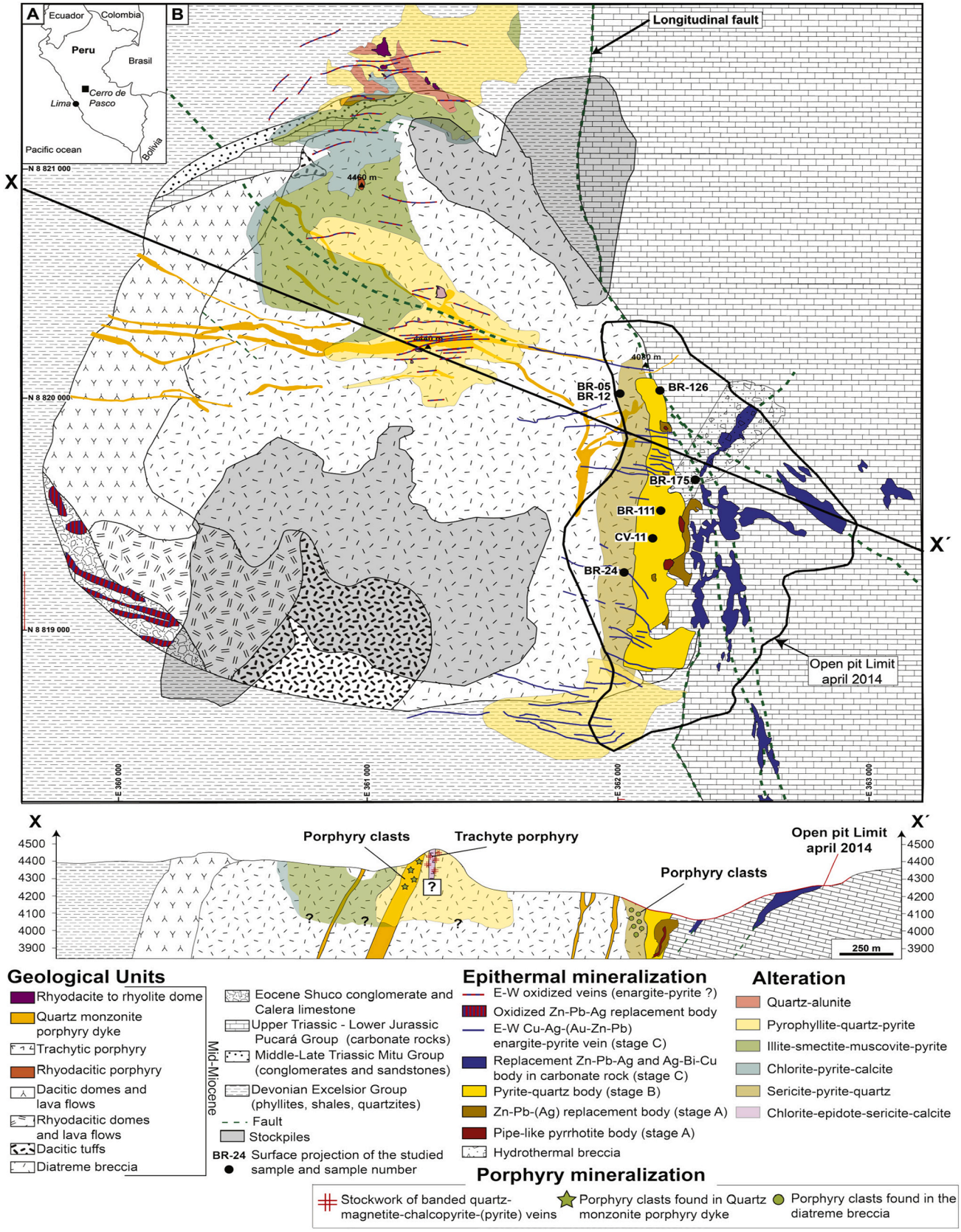

Fig. 1. Geological map and cross-section of the Cerro de Pasco diatreme-dome complex modified from Rottier et al. (2018a) that includes data from Rogers (1983), Baumgartner et al. (2008), and the Volcan's geological staff. A) Location of the Cerro de Pasco district, B) Geological map and surface projection of the samples used during this study.

and N150-trending fractures and plunging 25 to 60° west (Baumgartner et al., 2008). These bodies are well zoned laterally, with a high-sulfidation core including famatinite and alunite grading outwards to intermediate-sulfidation assemblages bearing Fe-poor sphalerite, galena and Ag- and Bi-sulfosalts and an outermost margin containing hematite (partially replaced by magnetite) and Fe-Mn-Zn carbonates (Baumgartner et al., 2008). Cross-cutting relationships combined with absolute age determinations indicate that the three epithermal polymetallic mineralization stages, from which only the late C_2 stage is dated (14.54 ± 0.08 to 14.41 ± 0.07 Ma, Ar-Ar on alunite; Baumgartner et al., 2009), postdated the different magmatic and porphyry mineralization events.

A detailed microthermometric and LA-ICP-MS study of fluid inclusions from the different mineralization stages was conducted by Rottier et al. (2018a) and allows reconstructing the salinity, the temperature, and the chemical evolution of the mineralizing fluids. The results are summarized in Table 1. The same study suggests that during mineralization stages A, B_1, B_2, and C_1 mixing of rising magmatic moderate-salinity metal-rich fluids (~20 wt% NaCl equiv.) with a surface-derived low-salinity fluid (< 2.5 wt% NaCl equiv.) stored below the paleowater table took place at mineralization site. The observed range of salinities requires that the magmatic fluids have been mixed with the surface-derived fluid in a proportion up to ~1:10. During stages A, B_1, and B_2, both fluids are thought to have roughly the same temperature as no temperature decrease has been recorded during dilution of the moderate-salinity metal-rich fluid (Rottier et al., 2018a). The origin of the surface-derived low-salinity fluid is uncertain and was interpreted as a mixture of condensed magmatic vapors and meteoric water (Rottier et al., 2018a). The enargite-pyrite veins of stage C_2 were interpreted to be formed by the ascent of CO_2-bearing contracted vapors, probably subsequently mixed with surface-derived fluid. Salinity of primary quartz-hosted fluid inclusion assemblages (FIAs) from the quartz-enargite veins of stage C_2 range between 1.2 and 2.7 wt% NaCl equiv. (Rottier et al., 2018a) which is significantly lower than for the other stages.

In this study to better define the origin of the mineralizing fluids and the mixing history, 10 quartz crystals from stages A, B_1, B_2 and C_2 were selected from the samples already studied by Rottier et al. (2018a), to perform in-situ SIMS oxygen isotope analyses combined with LA-ICP-MS trace element analyses.

3. Analytical methods

3.1. SEM-CL

Scanning electron microscopy cathodoluminescence (SEM-CL) was used to characterize texturally the studied quartz crystals. SEM-CL images were acquired at the University of Lausanne using a CamScan MV2300 SEM and at the University of Geneva using a JEOL JSM7001F SEM, both equipped with panchromatic CL detectors. The applied acceleration voltage and current were 15 kV and ~25 nA, respectively. The CL images were collected from one scan of 40-s acquisition speed and a processing resolution of 1280 × 960 pixels and 256 Gy levels.

3.2. SIMS

A total of 169 in-situ SIMS $^{18}O/^{16}O$ analyses were performed on 10 quartz chips placed in an indium mount together with grains of two quartz reference materials UNIL-Q1 for $\delta^{18}O$ measurements (Seitz et al., 2017). Measurements were performed at the SwissSIMS ion probe national facility at the University of Lausanne. Detailed procedures for $\delta^{18}O$ measurements are provided by Rottier et al. (2016b). The used setting allowed an average reproducibility better than 0.3‰ (2SD) on UNIL-Q1 reference material at the beginning of the session, and internal error for each analysis lower than 0.3‰ 2σ. A set of 4 analyses of UNIL-Q1 standard, inserted in the mount, has also been measured every 15–20 analyses for monitoring the instrument stability and assess the instrumental mass fractionation. Raw SIMS data and calculated $\delta^{18}O$ quartz values are reported in Supplementary Table A.1 and A.2. The variation of UNIL-Q1 over the entire session was below 0.3‰ (2SD). The 2SD bracket between the two sets of UNIL-Q1 standard analyses surrounding the analysis are also reported. The oxygen isotope composition of quartz is reported using the Vienna standard mean ocean water (VSMOW) as a reference.

3.3. LA-ICP-MS

A total of 111 laser ablation inductively coupled plasma mass spectrometry (LA-ICP-MS) spot analyses on 9 different quartz samples were acquired using a 193 nm ArF Excimer laser with an energy homogenized beam profile coupled with an ELAN 6100 DRC ICP quadrupole mass spectrometer (QMS) at ETH Zurich (Günther et al., 1997, 1998; Heinrich et al., 2003). The analytical conditions, data acquisition parameters, and list of isotopes analyzed are summarized in supplementary Table A.3. Quartz crystals were ablated using an iris diaphragm allowing a progressive manual increase of the laser beam diameter up to ~30 μm which limits explosion of the quartz during ablation (Guillong and Heinrich, 2007). LA-ICP-MS transient signals were reduced using the Sills software (Guillong et al., 2008). The limits of detection were calculated based on the method of Pettke et al. (2012). The NIST glass standard SRM 610 and quartz standard BGS-Q1 (Audétat et al., 2015) were analyzed both twice bracketing a maximum of 20 unknowns. NIST glass standard SRM 610 was used as an external standard and used to correct the drift by linear regressions, and accuracy of the analyses has been checked with the BGS-Q1 quartz standard. Obtained concentrations of Li (31 ± 1 ppm), Al (163 ± 6 ppm), Ti (53 ± 1 ppm), and Ge (1.6 ± 0.3 ppm) for the BGS-Q1 quartz standard are in the range of the reported values: Li (30 ± 2 ppm), Al (154 ± 15 ppm), Ti (57 ± 4 ppm), and Ge (1.7 ± 0.2 ppm; Audétat et al., 2015). Phosphorous, Ca, and Sn are strongly affected by mass interferences or contamination (Flem and Müller, 2012; Schlöglova et al., 2017). Obtained concentrations of these elements are generally constant during a single session regardless of the sample, suggesting that they reflect these mass interferences or contamination, and thus, they were discarded.

Table 1
Summary of the main results from the fluid inclusion study of Rottier et al. (2018a). (*) Average homogenization temperature (Th) for stage C_1 is not reported in reason of the large range of measured Th.

Mineralization stage	Number of fluid inclusions/FIAs	Host mineral	Range of homogenization temperatures (°C)	Average homogenization temperature (°C) for primary quartz-hosted FIAs	Range of salinities (wt% NaCl equiv.)
A	201/25	Sl, Qtz	220–280	250	2.5–16.0
B1	120/15	Qtz	230–360	260	3.1–18.5
B2	302/35	Qtz	220–280	240	2.7–16.2
C1	257/29	Sl, Cb	150–280	*	1.1–19.1
C2	142/18	En, Qtz	190–295	270	1.2–2.7

Abbreviations: Cb – carbonate; En – enargite; FIA – fluid inclusion assemblage; Qtz – quartz; Sl – sphalerite.

4. Results

4.1. General description

Idiomorphic to subidiomorphic quartz from 7 different samples of mineralization stages A, B_1, B_2 and C_2 was selected for in-situ SIMS oxygen isotope and LA-ICP-MS analyses. No suitable stage C_1 quartz was found. In all selected samples, quartz occurs texturally intergrown with the main sulfides or sulfosalts characteristic of each mineralization stage, a detailed description of the samples is provided in supplementary Table A.4. Prior selection of the quartz portions where the in-situ SIMS oxygen isotope and LA-ICP-MS trace element analyses would be performed, a careful SEM-CL textural study was done to avoid inclusions and to select the analysis points as much as possible along transects across crystal growth zones. Results of the in-situ SIMS oxygen isotope and LA-ICP-MS analyses are summarized in Table 2 and Table 3, respectively. The entire datasets are available in supplementary Tables A.1, A.2, and A.5.

The obtained $\delta^{18}O_{quartz}$ values range from 4.6 to 20.4‰ and significant variations, up to 11.5‰, are observed within single quartz crystals from the different mineralization stages (A, B_1, B_2 and C_2; Table 2; Fig. 2). Such $\delta^{18}O_{quartz}$ variations were not recorded by the previous study, using bulk oxygen isotope analyses (Fig. 2) of quartz separates of stage A ($\delta^{18}O_{quartz} = 15.3$ and 15.8‰), B_2 ($\delta^{18}O_{quartz} = 16.0$–17.2‰, $n = 3$) and C_2 ($\delta^{18}O_{quartz} = 10.8$–13.3‰, $n = 4$) performed by Baumgartner et al. (2008). However, for the different stages (A, B_2, and C_2) the obtained $\delta^{18}O_{quartz}$ from the bulk analyses are close to the average $\delta^{18}O_{quartz}$ compositions obtained by SIMS on quartz crystals belonging to the same stage (Fig. 2). The $\delta^{18}O_{H2O}$ values, estimated isotopic composition of the fluid in equilibrium with quartz during precipitation ranges between −3.8 and 10.9‰ (Fig. 2). These were calculated assuming that isotopic equilibrium was maintained between quartz and fluid during quartz precipitation, an assumption discussed later. The $\delta^{18}O_{H2O}$ values were calculated using the average homogenization temperatures of FIAs from each mineralization stages (Table 1) as measured by Rottier et al. (2018a) and using the fractionation factors of Zheng (1993). In shallow environments (< 1 km deep), such as Cerro de Pasco, homogenization temperatures can be considered as a good approximation of quartz crystallization temperatures (i.e., trapping temperatures; Rottier et al., 2018a). Measured homogenization temperatures show little variation between the different mineralization stages (Table 1). Temperature variations observed between stages A and B_2 are, at most, of 60 °C (from 220 to 280 °C; Table 1) yielding, at most, a 2.7‰ difference on the calculated $\delta^{18}O_{H2O}$ (Zheng, 1993). Temperature variations within stages B_1 (240–280 °C) and C_2 (260–295 °C) are smaller and would lead to differences of 1.7 and 1.3‰, respectively. Fig. 2 also displays the range of SIMS $\delta^{18}O_{quartz}$ and calculated $\delta^{18}O_{H2O}$ values obtained on quartz of PM1 and PM2 porphyry-type veins previously published by Rottier et al. (2016b) and (Rottier et al., 2018b).

Table 3
Summary of trace element content ranges obtained by LA-ICP-MS analyses on quartz crystals from the different mineralization stages in this study (min-max values, in ppm).

	Stage A	stage B_1	Stage B_2	Stage C_2
Li (ppm)	7.5–17.9	1.1–16.4	0.7–5.6	1.0–1.7
B (ppm)	8.4–15.2	2.9–16.4	4.2–11.4	<5.1–7.7
Na (ppm)	1.6–49.7	0.3–4	0.7–14.5	1.0–2.7
Mg (ppm)	1.0–35.7	<0.3–68.0	<0.5–1.8	<0.5
Al (ppm)	1237–1818	43.4–1981	289–2098	45.5–351
K (ppm)	<13.4–158	<9.6	<8.5–60.7	<10.2
Ti (ppm)	<1.8–2.1	0.8–10	1.0–7.5	<1–4.9
Fe (ppm)	<11–29.7	<4.0–12.9	<6.4–44.8	<14.4
Ga (ppm)	4.3–15.8	<0.04–1.6	0.1–1.7	<0.04–0.5
Ge (ppm)	6.5–23.6	<1.2–7.6	3.3–15.8	<0.8–2.6
As (ppm)	<1.5	0.3–8.6	<0.4–110	<0.6–10
Rb (ppm)	<0.04–1.4	<0.02–0.1	<0.03–0.8	<0.03–0.03
Sr (ppm)	<0.03–0.82	<0.02–0.03	<0.02–0.2	<0.02–0.2
Sb (ppm)	24.8–59.8	0.6–81.8	2.2–100	1.1–4.9

Quartz crystal from the different mineralization stages display variable trace element concentrations (Table 3, supplementary Table A.5, Fig. 3). Aluminum is the most abundant and variable trace element, with concentrations ranging from 43.4 to 2098 ppm, with values <500 ppm restricted to stages B_1 and C_2 (Figs. 3A-F). Lithium shows good correlation with Al (Fig. 3A); values of quartz crystals from mineralization stages A, B_1, and C_2 plotting along a same broad trend, and those from stage B_2 plotting along a parallel trend characterized by lower Li contents (Fig. 3A). Titanium, Sb, and Ge exhibit a rough correlation with Al for quartz from stages B_1, B_2 and C_2 (Figs. 3B-D). A correlation between Al and Ga exists for quartz from stage B_2 (Fig. 3E). The sodium content of the analyzed quartz is low (95% of the analyses <8 ppm; Fig. 3F) and does not correlate with any other element, which suggests that contamination by fluid inclusions, if any, is negligible (Rottier and Casanova, 2020).

Table 2
Range of measured $\delta^{18}O$ (‰) values in quartz crystals. Microthermometric data obtained by Rottier et al. (2018a) on the same sample (not necessarily the same quartz crystal) are also reported. Only primary and pseudosecondary fluid inclusion assemblages (FIA) are reported, except for sample BR-12 Q5 where only secondary fluid inclusions were studied.

Sample #	Mineralization stage	Number of analytical $\delta^{18}O$ spots	Range of measured $\delta^{18}O$ (‰)	Figure	Number of FIA	Salinity (wt% NaCl equiv.)		Homogenization temperature (°C)	
						min	max	min	max
BR-111	A	20	11.2–19.4	Fig. 4	4	6.9 ± 0.2	15.2 ± 0.1	249 ± 7	261 ± 7
BR-175	A	10	14.7–17.6	Fig. A.1[a]	4	2.7 ± 0.2	15.3 ± 0.4	186 ± 2	255 ± 11
BR-12 Q2	B_1	37	4.65–16.12	Fig. 5	1	6.2 ± 0.3		240 ± 9	
BR-12 Q5	B_1	10	13.9–16.3	Fig. A.2[a]	1	(18.3 ± 0.9)[b]		(358 ± 11)[b]	
BR-05 Q1	B_1	6	14.0–17.9	Fig. A.2[a]	5	5.3 ± 0.5	18.36 ± 0.3	248 ± 4	306 ± 7
CV-11 Q6	B_2	37	8.7–19.6	Fig. 5	7	2.9 ± 0.9	8.6 ± 0.1	209 ± 7	261 ± 2
CV-11 Q7	B_2	8	12.0–19.2	Fig. A.3[a]	1	5.5 ± 0.2		264 ± 5	
BR-126	B_2	13	12.9–20.4	Fig. 7	1	5.8 ± 0.4		250 ± 4	
BR-24 Q1	C_2	23	7.6–18.5	Fig. 8	1	1.1 ± 0.1		294 ± 1	
BR-24 Q2	C_2	5	5.9–14.4	Fig. A.4[a]	5	2.1 ± 0.3	2.5 ± 0.3	265 ± 15	291 ± 19

[a] Figures available in the supplementary files.
[b] Secondary fluid inclusions.

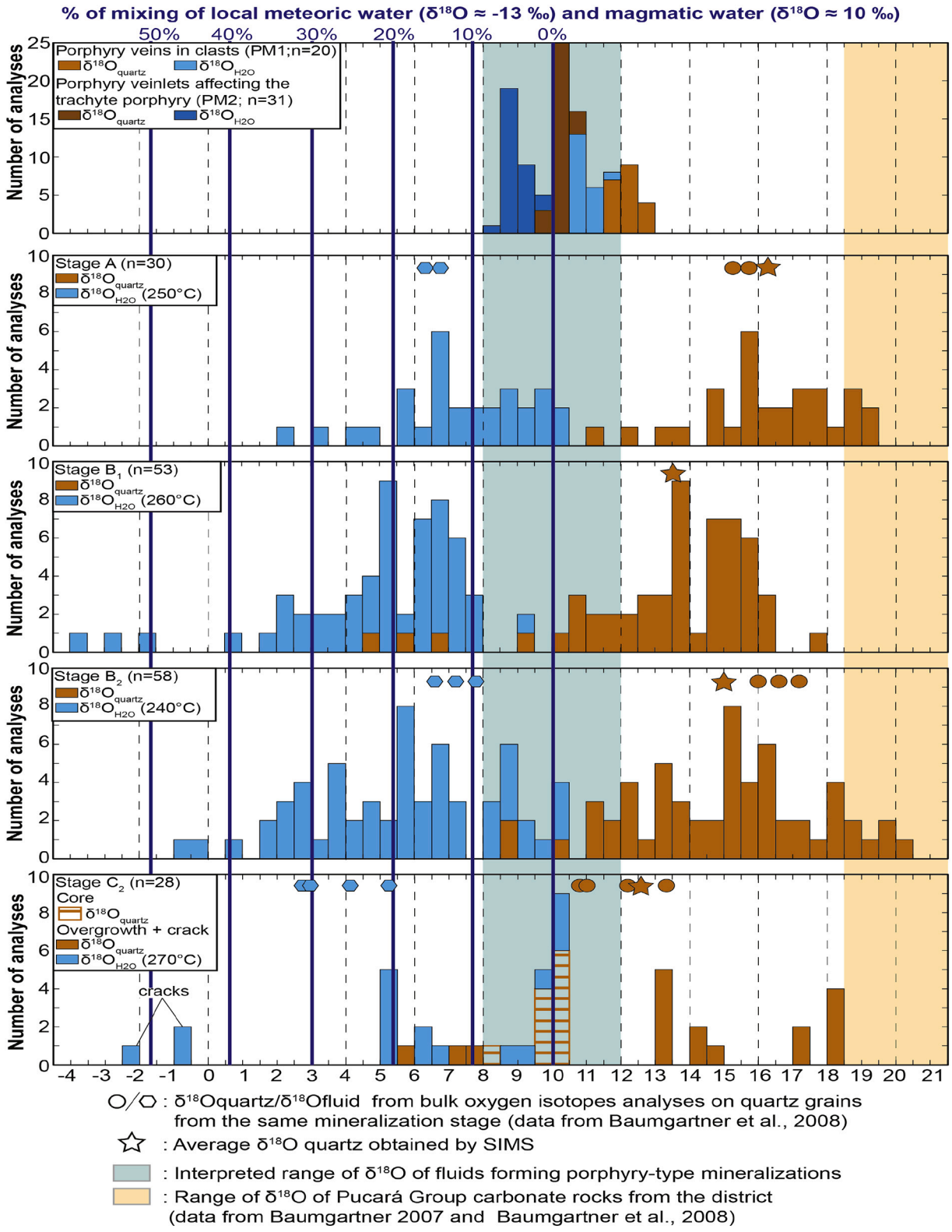

Fig. 2. Histogram of in-situ $\delta^{18}O$ isotopic compositions of quartz obtained from the different epithermal mineralization stages (A, B_1, B_2 and C_2) and of the corresponding fluids (calculated with the average temperatures of Table 1). The range of $\delta^{18}O$ of fluids forming porphyry-type mineralization is from SIMS data by Rottier et al. (2016b) and (Rottier et al., 2018b).

4.2. Sample description

In the following sample description, to better track the evolution of the quartz oxygen isotope and trace element composition during crystal growth, the results of the analyses have been projected on lines parallel or perpendicular to the crystal *c*-axis by following the growth bands as revealed by CL luminescence (Figs. 4 to 8). It should be taken into account that the growth bands are. in places, smaller than the spot size of

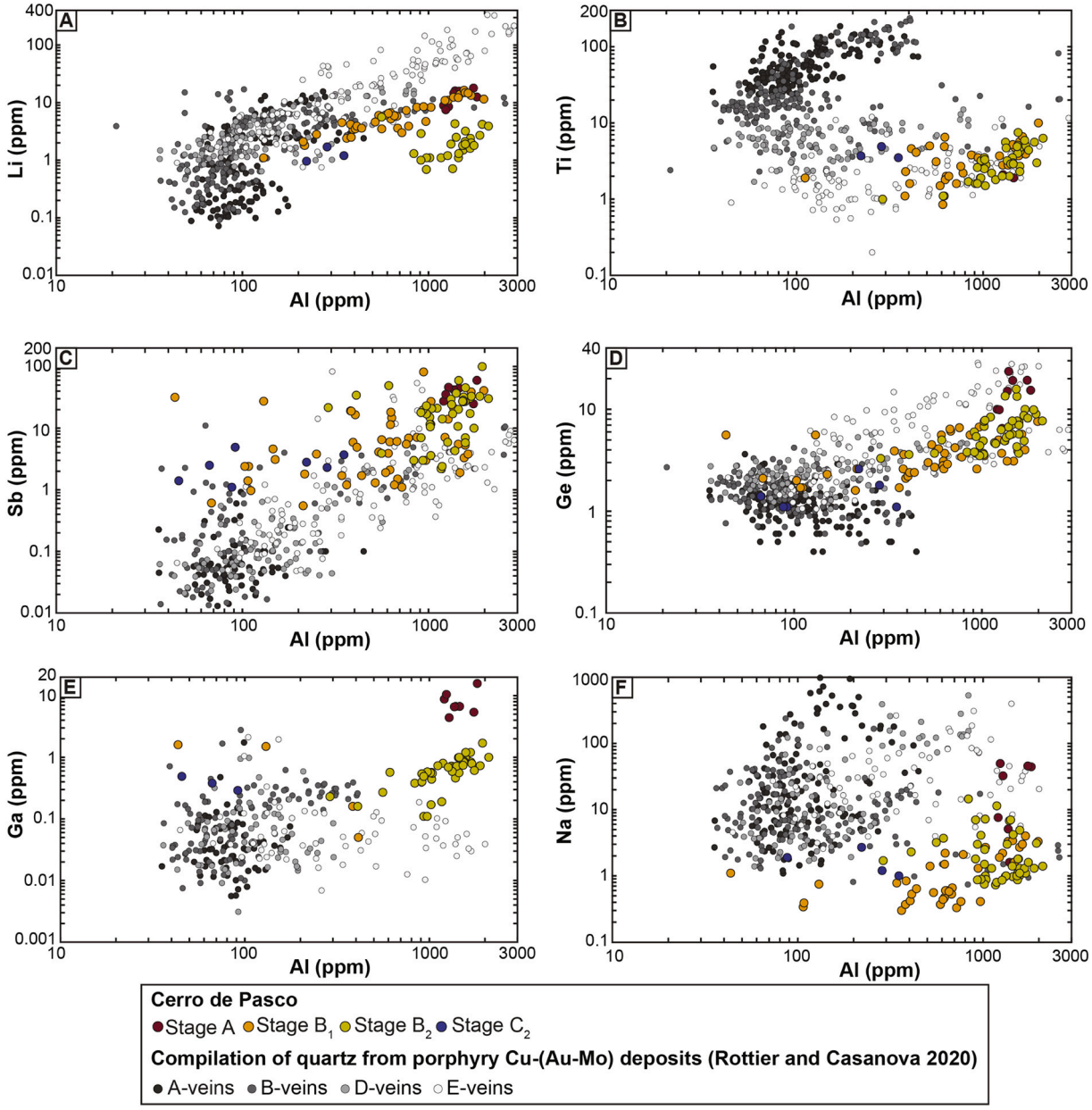

Fig. 3. Correlation plots of selected trace elements (Li, Ti, Sb, Ge, Ga and Na) in quartz of stages A, B_1, B_2, and C_2 versus Al (values in supplementary Table A.2). Data from A-, B-, D-, and *E*-veins are from the compilation of Rottier and Casanova (2020).

SIMS analyses (~15 μm), itself smaller than the one used for the LA-ICP-MS analyses (~30 μm). Therefore, caution is also needed when comparing the values obtained with both methods.

4.2.1. Stage A

Two samples from mineralization stage A were analyzed, BR-111 and BR-175; they consist of Fe-rich sphalerite, galena, pyrrhotite, pyrite, and quartz. Quartz in both samples is euhedral to subhedral and displays fine oscillatory growth zoning characterized by low- to high-CL intensity (Fig. 4A and supplementary Fig. A.1). In these two figures areas with very high-CL intensity are due to apatite inclusions. The $\delta^{18}O_{quartz}$ values of sample BR-111 vary between 11.2 and 19.4‰, mostly ranging between 14.6 and 19.4‰ (Fig. 4A and B). A detailed transect realized through this quartz crystal shows a $\delta^{18}O_{quartz}$ plateau around ~19‰ in its inner part (Fig. 4B, profile A-B) followed by a sharp $\delta^{18}O_{quartz}$ drop from 18.9 to 11.2‰ in less than 30 μm; then the $\delta^{18}O_{quartz}$ values vary between 13.1 and 15.8‰. The rim of the crystal has a $\delta^{18}O_{quartz}$ value of 18‰ (Fig. 4B, profile A-B). Trace element analyses by LA-ICP-MS performed along a profile parallel to that of oxygen isotope analyses show only diffuse correlation with the obtained $\delta^{18}O_{quartz}$ values (Figs. 4C and D). The sharp drop of $\delta^{18}O_{quartz}$ from 18.9 to 11.2‰ does not correlate with a sharp decrease in Al, Li, Ge, or Sb content. However, a slight decrease of the Al, Li, Ge, and Sb content is observed from the inner part of the crystal, characterized by $\delta^{18}O_{quartz}$ ~19‰, to its external part that shows more variable $\delta^{18}O_{quartz}$ values between ~18 and 11‰ (Fig. 4C and D). Sample BR-175 shows a smaller range of $\delta^{18}O_{quartz}$ values than BR-111, the obtained $\delta^{18}O_{quartz}$ values varying between 14.7 and 17.6‰ (supplementary Fig. A.1). In both samples, no correlation between the obtained $\delta^{18}O_{quartz}$ and CL intensity was observed (Fig. 4A-D and supplementary Fig. A.1).

4.2.2. Stage B_1

Three quartz crystals (BR-12 Q2, BR-12 Q5, and BR-05 Q1) from two different samples of quartz-pyrite-chalcopyrite B_1 veins were analyzed.

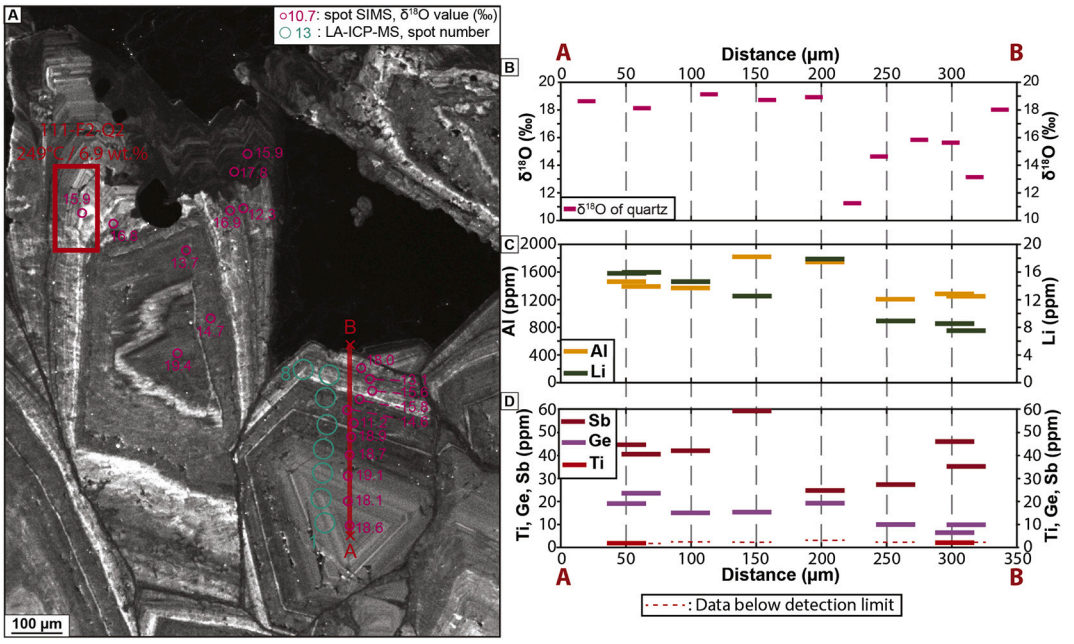

Fig. 4. A) SEM-CL image of quartz grains from stage A sample BR-111. The red rectangle define the footprint of the studied fluid inclusions assemblage (FIA), FIA number and obtained average salinity and homogenization temperature are reported; B) $\delta^{18}O$ composition of quartz and of the fluid in equilibrium with it calculated using the equation of Zheng (1993), assuming a temperature of 250 °C, along the profile A-B; C and D) Selected trace element concentrations obtained by LA-ICP-MS along profile A-B. The width of the horizontal bars corresponds to the size of the SIMS and LA-ICP-MS spots. (For interpretation of the references to colour in this figure legend, the reader is referred to the web version of this article.)

The three quartz crystals are euhedral and present fine oscillatory growth zoning characterized by low- to high-CL intensity (Fig. 5A and supplementary Fig. A.2).

A total of 38 $\delta^{18}O$ SIMS and 27 LA-ICP-MS spot analyses were performed on quartz crystal BR-12 Q2 (Fig. 5A). Based on the obtained $\delta^{18}O_{quartz}$, three distinct zones were defined (inner/intermediate/tip; Fig. 5A and B). The inner part of the crystal has $\delta^{18}O_{quartz}$ values between 13.4 and 16.1‰. In this part, two $\delta^{18}O_{quartz}$ drops defined by three points (at ~900 and ~1350 µm, Fig. 5B) are observed. The ~3‰ drop at ~900 µm is outlined by two values, 11.9‰ and 12.9‰ and occurs over more than 50 µm (Fig. 5A and B). The second drop is sharper, from 15.0 to 4.6‰, and is followed by an increase to 13.4‰ of the $\delta^{18}O_{quartz}$ over ~100 µm (Fig. 5A, B). The intermediate zone of the quartz is characterized by lower $\delta^{18}O_{quartz}$ values (between 9.1 and 13.1‰) showing some scattering (Fig. 5A and B). The limit with the tip of the crystal ($\delta^{18}O_{quartz}$ values between 6.8 and 5.8‰) is sharp. The LA-ICP-MS trace element analyses show large variations of Al, Ti, Li, Ge, and Sb contents (Fig. 5C and D). The two $\delta^{18}O_{quartz}$ drops observed in the inner part of the crystal correlate with marked decrease of the Al, Li, and Ti contents; Sb and Ge show less clear trends (Fig. 5B-D). The intermediate part and the tip display lower Al, Li, and Ge contents than those from the inner crystal part; no specific variation of the Ti and Sb content is observed (Fig. 5C and D).

A smaller number of in-situ SIMS oxygen isotope and LA-ICP-MS trace element analyses were done on the two other crystals from this B_1 mineralization stage (BR-05 Q1 and BR-12 Q5). All SIMS oxygen isotope analyses were performed in parts equivalent to the inner part of the crystal BR-12 Q2 (supplementary Fig. A.2). The $\delta^{18}O_{quartz}$ values vary from 13.9 to 16.3‰ and from 14 to 17.9‰ for BR-05 Q1 and BR-12 Q5, respectively (supplementary Fig. A.2), a similar span to that observed in the inner part of crystal BR-12 Q2. In all quartz crystals of this stage B_1, no correlation between the obtained $\delta^{18}O_{quartz}$ and CL intensity nor with the quartz texture was noticed.

4.2.3. Stage B_2

Four crystals from mineralization stage B_2 were analyzed: CV-11 Q6a, CV-11 Q6b, CV-11 Q7, and BR-126. They were selected from two samples of the massive pyrite-quartz body replacing Pucará carbonate rocks. Like for stage B_1, quartz crystals are euhedral and display fine oscillatory growth zoning characterized by low- to high-CL intensities (Figs. 6A, 7A, and supplementary Fig. A.3). Sample CV-11 Q6 is composed of two adjacent quartz crystals Q6a and Q6b (Fig. 6A). The core of crystal Q6a (0–300 µm) is characterized by relatively low and variable $\delta^{18}O_{quartz}$ values between 8.7 and 13.2‰ (Fig. 6A, B), then, a steady increase up to 18.9‰ is observed (300–600 µm; Fig. 6A, B), followed by a progressive decrease to values down to 11.5‰ (600–750 µm). Around 780 µm, the $\delta^{18}O_{quartz}$ value jumps to 19.6‰ before progressively decreasing down to 12‰ (Fig. 6A, B). Trace element LA-ICP-MS analyses performed on the same crystals reveal strong variations in Al, Li, Ti, Sb, and Ge content; no correlation with the measured $\delta^{18}O_{quartz}$ values is recognized (Fig. 6B-D).

Eight $\delta^{18}O_{quartz}$ values were obtained for crystal CV-11 Q7. It belongs to the same sample as quartz crystal CV-11 Q6 (supplementary Fig. A.3). It also shows a core characterized by low $\delta^{18}O_{quartz}$ at ~12‰, followed by an increase to 17.8‰, a drop at 14.2‰, an increase to 19.6‰, and a final drop at 15.4‰ (supplementary Fig. A.3). As for quartz CV-11 Q6, quartz crystal CV-11 Q7 shows strong variations of Al, Li, Ti, Sb and Ge content without clear correlation with the obtained $\delta^{18}O_{quartz}$ (supplementary Fig. A.3).

Thirteen $\delta^{18}O_{quartz}$ values were obtained from quartz crystal BR-126 (Fig. 7A). The core of the crystal was not analyzed. Most values are between 12.9 and 16.8‰ (Fig. 7A, B), showing several up and downs, the crystal tip showing high $\delta^{18}O_{quartz}$ value at 20.4‰ (Fig. 7A, B). As in the other quartz crystals from stage B_2, the obtained trace element contents are variable and show no correlation with the obtained $\delta^{18}O_{quartz}$ values (Fig. 7B-D).

4.2.4. Stage C_2

Two quartz crystals from an enargite-pyrite vein (stage C_2) were analyzed. Quartz grain BR-24 Q1 shows complex CL texture, with homogeneous low-CL intensity core, overgrown by moderate to high-CL intensity well-zoned quartz (Fig. 8A); this overgrowth often contains

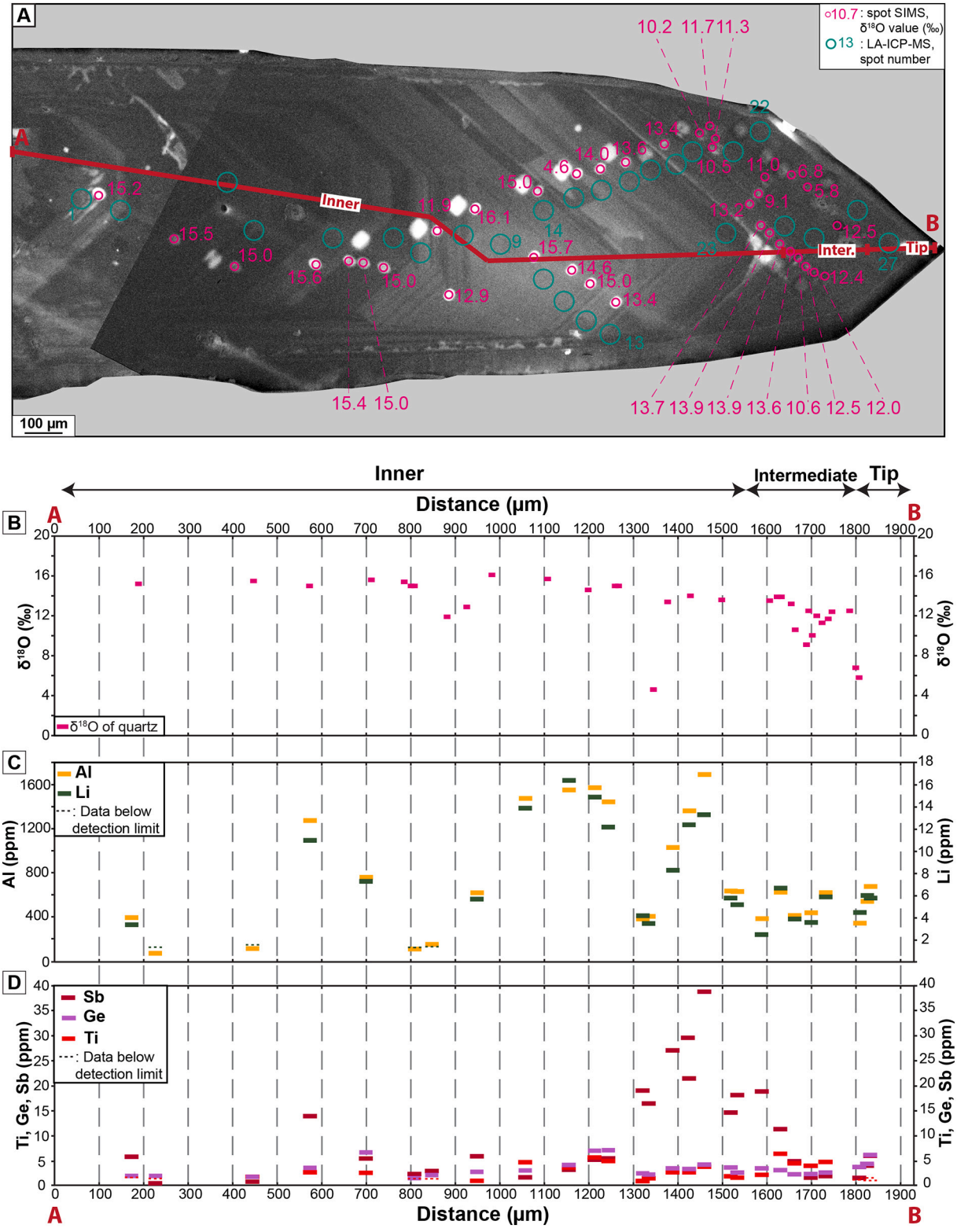

Fig. 5. A) SEM-CL image of quartz crystal BR-12 Q2 from stage B_1; B) $\delta^{18}O$ composition of quartz along profile A-B; C and D) Selected trace element concentrations obtained by LA-ICP-MS along profile A-B-C. The width of the horizontal bars corresponds to the size of the SIMS and LA-ICP-MS spots.

small solid inclusions (< 10 µm) of alunite and clay minerals. Quartz core and its overgrowth are crosscut by cracks filled by low-CL intensity quartz (Fig. 8A). The dark core displays homogeneous low $\delta^{18}O_{quartz}$ values varying between 9.7 and 10.4‰, whereas the overgrowth shows more complex signatures. The overgrowth analyzed in profile C-D (Fig. 8C) shows constant $\delta^{18}O_{quartz}$ at ~18.5‰, decreasing to 14.3‰ near the rim. The overgrowth analyzed in profile A-B (Fig. 8B) presents highly variable $\delta^{18}O_{quartz}$ values between 9.8 and 18.3‰. Two analyses performed on the dark quartz filling cracks yield the lowest $\delta^{18}O_{quartz}$ values of 7.3 and 8.4‰ (Fig. 8A, B). Trace element LA-ICP-MS analyses yield low Al (< 100 ppm) and Ti (< 1 ppm) content for the dark crystal core, whereas compositions of the moderate- to high-CL intensity

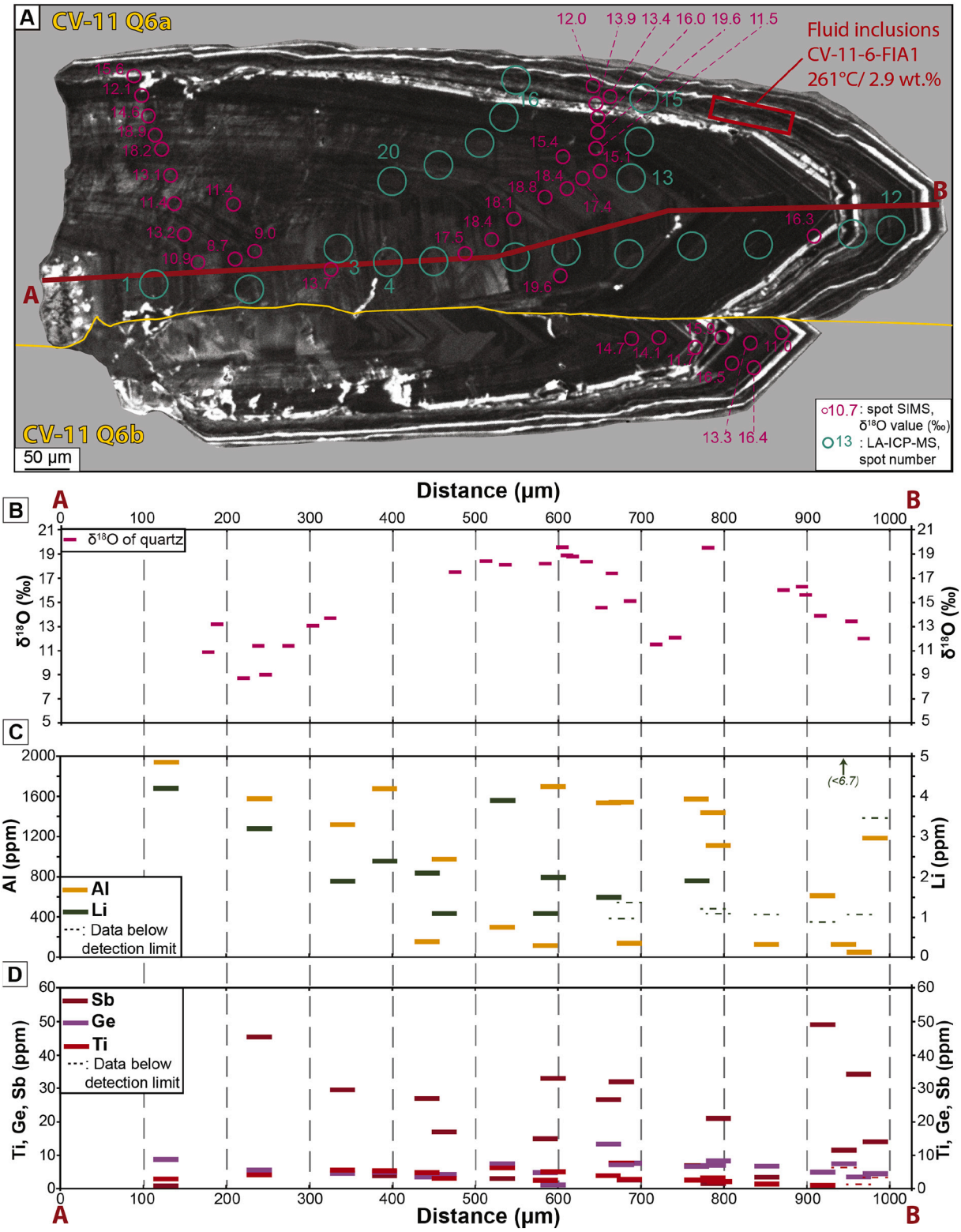

Fig. 6. A) SEM-CL image of quartz crystal CV-11 Q6 from stage B_2. The red rectangle define the footprint of the studied fluid inclusions assemblage (FIA), FIA number and obtained average salinity and homogenization temperature are reported B) $\delta^{18}O$ compositions of quartz and of fluid in equilibrium with it calculated using the equation of Zheng (1993) and assuming a temperature of 245°, along the profile A-B; C-D) Selected trace element concentrations obtained by LA-ICP-MS along profile A-B; The width of the horizontal bars corresponds to the size of the SIMS and LA-ICP-MS spots. (For interpretation of the references to colour in this figure legend, the reader is referred to the web version of this article.)

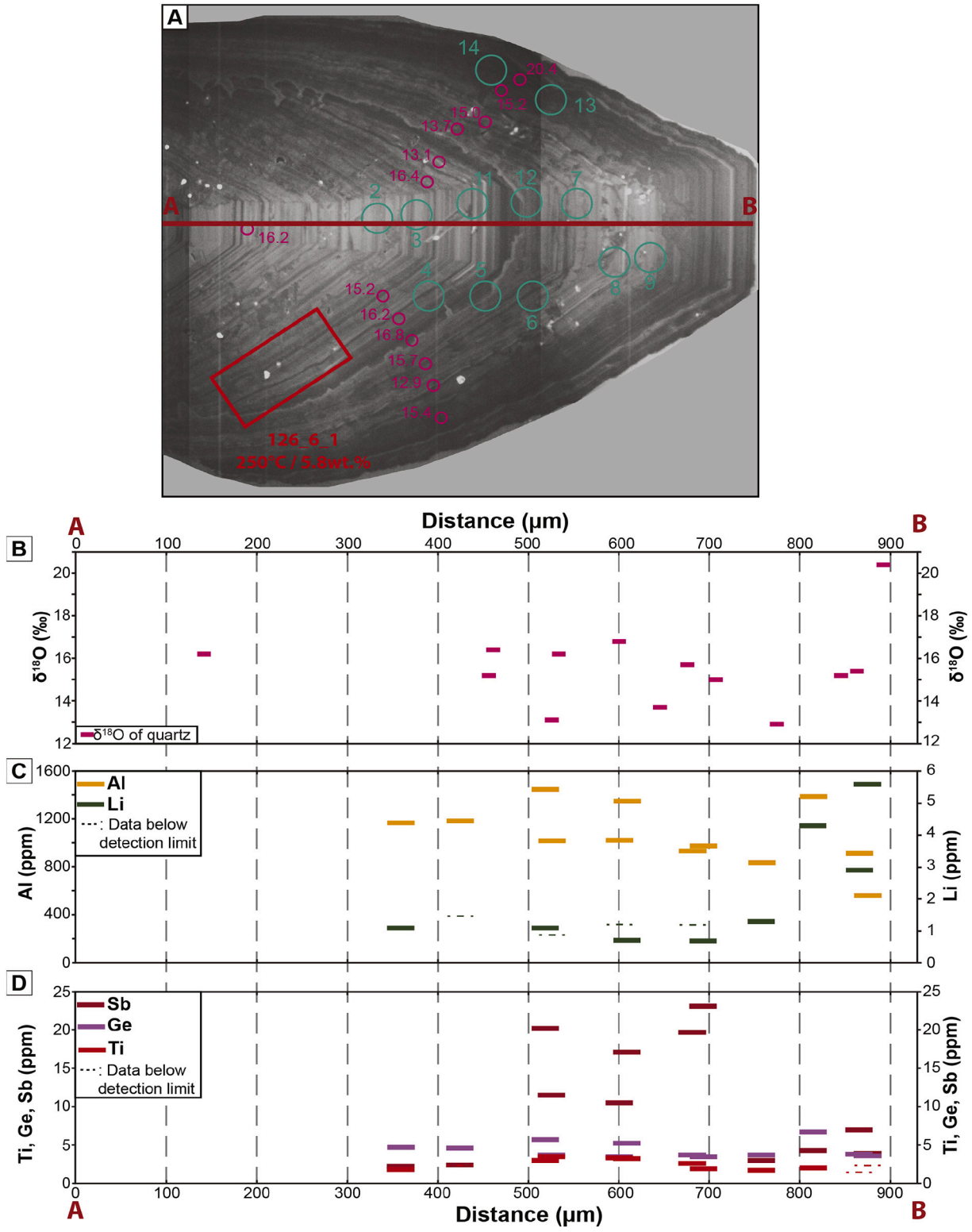

Fig. 7. A) SEM-CL image of quartz crystal BR-126 from stage B_2. The red rectangle define the footprint of the studied fluid inclusions assemblage (FIA), FIA number and obtained average salinity and homogenization temperature are reported. B) $\delta^{18}O$ composition of quartz and of fluid in equilibrium with it calculated using the equation of Zheng (1993) and assuming a temperature of 245 °C along the profile A-B. C-D) Selected trace element concentrations obtained by LA-ICP-MS along profile A-B; The width of the horizontal bars corresponds to the size of the SIMS and LA-ICP-MS spots. (For interpretation of the references to colour in this figure legend, the reader is referred to the web version of this article.)

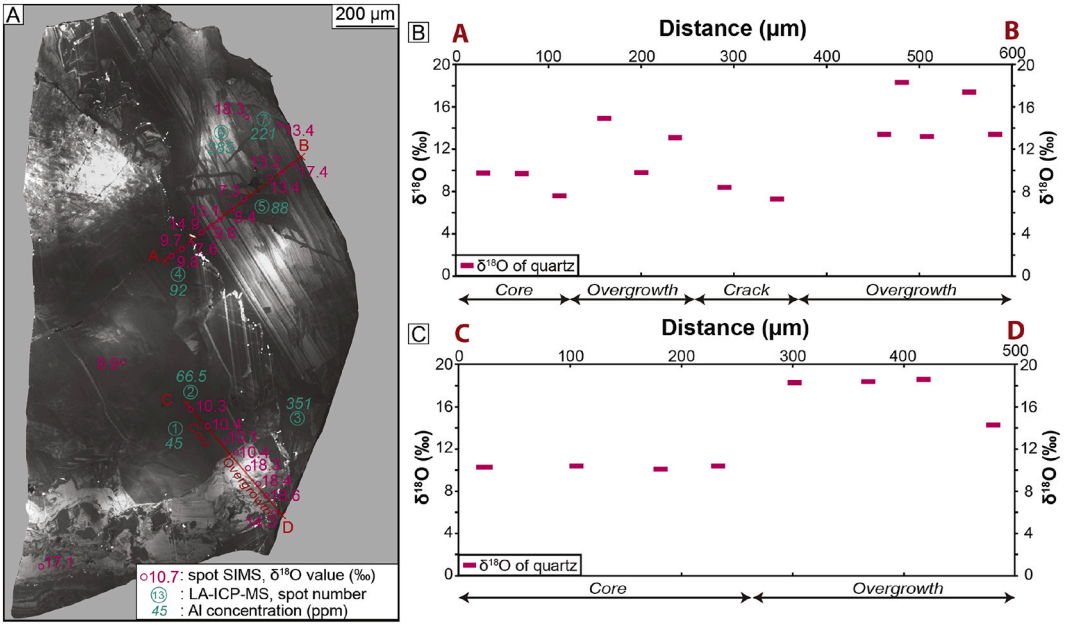

Fig. 8. A) SEM-CL image of quartz grain BR-24 Q1 from stage C_2; B-C) $\delta^{18}O$ composition of quartz along profiles A-B (B) and C-D (C). The width of the horizontal bars corresponds to the size of the SIMS spots.

overgrowth are strongly variable and are higher in Al (up to 350 ppm) and Ti (up to 4.9 ppm, Fig. 8A; supplementary Table A.5). The dark healed fractures also display low Al and Ti contents with 88 ppm and < 1 ppm, respectively (Fig. 8A; supplementary Table A.5).

Quartz grains from sample BR-24 Q2 present numerous cores of xenocrystic magmatic quartz grains characterized by high-CL intensity (supplementary Fig. A.4). These magmatic cores are crosscut and overgrown by low- to moderate-CL intensity well-zoned quartz. The magmatic quartz grains display $\delta^{18}O_{quartz}$ values of 10.4 and 10.5‰ (n = 2) whereas the three analyses performed on the overgrowth yield $\delta^{18}O_{quartz}$ values of 14.4, 13.4 and 5.9‰ (supplementary Fig. A.4).

5. Discussion

5.1. Trace elements in hydrothermal quartz

Quartz SEM-CL images reveal well-developed oscillatory zoning (Figs. 4 to 8; supplementary Figs. A.1 to A.4). Variation of luminescence intensity observed in hydrothermal quartz is attributed to compositional differences (Landtwing and Pettke, 2005; Jourdan et al., 2009b; Lehmann et al., 2011; Rusk et al., 2011; Rusk, 2012). For most studied quartz crystals, the growth band thickness revealed by the SEM-CL imaging is smaller than the spot size used for the LA-ICP-MS and SIMS analyses (Figs. 4 to 8; supplementary Figs. A.1 to A.4), thus limiting the possibility to link variations of a specific trace element contents or $\delta^{18}O_{quartz}$ values to the CL luminescence of a particular band. Covariations between trace element content and quartz oxygen isotope composition have been observed in quartz crystals BR-12 Q2 and BR-24 Q1 from stages B_1 and C_2, respectively (Figs. 5A-D and 8A). The two sharp drops in the oxygen isotope composition observed in the inner part of the quartz BR-12 Q2 are associated to a drop in the Al and Li content (Figs. 5A-D). The low CL-luminescent core and cracks of quartz BR-24 Q1 are characterized by low $\delta^{18}O_{quartz}$ composition and by lower Al, Li, Ti, and Ge content compared to the overgrowth which is high CL-luminescent and has heavier $\delta^{18}O_{quartz}$ (Fig. 8A). These observations suggest that the composition of the different mineralizing fluids at the origin of the variable oxygen isotope composition observed in quartz BR-12 Q2 and BR-24 Q1 have also controlled the trace element signature of this quartz. However, no such covariation between strong isotopic composition changes and trace element composition of the quartz is observed in the other quartz samples (Figs. 4A-D, 6A-D and 7A-D). This suggests that other factors control the trace element incorporation in quartz including physical (pressure and temperature) and chemical parameters (pH, Eh, fluid composition), and growth rate (Rottier and Casanova, 2020). One or a combination of these factors can be responsible for the observed variations. As mentioned above, the interpretation of the data is also limited by the spot size of the LA-ICP-MS measurements, larger than most of the quartz growth bands. Despite this, some general observations can be made.

Quartz from Cerro de Pasco display similar chemical composition than quartz from epithermal deposits and from late low-temperature (< 350 °C) veins of porphyry Cu-(Au-Mo) deposits (*E*-veins; Fig. 3), and they show a higher Al, Sb, Ge, and Ga and lower Ti content than quartz from A, B, and D veins from porphyry Cu-(Au-Mo) deposits according to the compilation done by Rottier and Casanova (2020). All studied quartz crystals from Cerro de Pasco show a good linear correlation between Al and Li contents (Fig. 3A). Even though Al concentration is strongly variable inside the different analyzed quartz crystals, a rough decrease of Al content from stages A, B_2, B_1, to C_2 is observed (Fig. 3, Table 3). Some studies suggest that the Al content of quartz negatively correlates with pH of the mineralizing fluids (Allan and Yardley, 2007; Rusk et al., 2008). This negative correlation is not supported by the data obtained in this study as the pH of the mineralizing fluids decreases from stage A, B_2, B_1 to C_2 based on alteration mineral assemblages (Baumgartner et al., 2008; Rottier et al., 2016a; Rottier et al., 2018a). Quartz from stage B_2 shows significantly lower Li for similar Al contents than quartz from the other stages (Fig. 3A). The microthermometry and LA-ICP-MS fluid inclusion studies performed by Rottier et al. (2018a) do not reveal Li content, temperature, and pressure variations between the different stages suggesting that Li incorporation into the quartz lattice at Cerro de Pasco is not directly controlled by the Li concentration, the temperature, or the pressure of the hydrothermal fluid, and that an unrecognized factor should affect the Li incorporation into the quartz structure.

Titanium incorporation in quartz is known to be dependent on pressure, temperature, Ti activity of the mineralizing fluids, and on quartz growth rate (Wark and Watson, 2006; Thomas et al., 2010; Huang and Audétat, 2012; Zhang et al., 2020). Different equations linking the Ti content to precipitation temperature and pressure of

quartz have been developed (Thomas et al., 2010; Huang and Audétat, 2012; Zhang et al., 2020). Nonetheless, accuracy of this geothermobarometer is discussed for hydrothermal quartz notably in reason of the role played by the quartz growth rate on the Ti content (Huang and Audétat, 2012; Rottier et al., 2018b). At Cerro de Pasco, the mineralization emplacement depth and the quartz precipitation temperatures for each mineralization stage are well constrained (Rottier et al., 2018a). Moreover, the presence of solid inclusions of rutile and/or anatase in the studied quartz crystals (Rottier et al., 2016a and Rottier et al., 2018a) buffers the titanium activity of the fluid at 1. Estimated quartz precipitation temperatures have been calculated using the published equations of Thomas et al. (2010), Huang and Audétat (2012), and Zhang et al. (2020). The calculated temperatures using the equations of Thomas et al. (2010) and Huang and Audétat (2012) are always higher (up to 80 °C) than the temperatures obtained from fluid inclusion microthermometry (Table 4). In contrast, the temperatures obtained with the equation of Zhang et al. (2020) are generally lower (up to 60 °C; Table 4). For certain applications, this error can be considered as acceptable but at the considered temperatures of <350 °C, such temperature overestimation or underestimation strongly affects the interpretation of the oxygen isotope signature of the fluid in equilibrium with quartz, due to the strong influence of temperature on isotopic fractionation between quartz and water at such moderate to low temperatures (Zheng, 1993).

5.2. Fluids involved in the magmatic-hydrothermal system at Cerro de Pasco

5.2.1. Factors influencing the $\delta^{18}O$ composition of quartz

As mentioned above, the $\delta^{18}O_{H2O}$ reported on Fig. 2 have been calculated assuming that isotopic equilibrium was maintained between quartz and fluid during quartz precipitation. If precipitation took place out of equilibrium, precipitated quartz will be enriched in the heavier ^{18}O isotope resulting of higher $\delta^{18}O_{quartz}$ values than under equilibrium condition (e.g., Clayton and Mayeda, 2009). Equilibrium precipitation of a growth band is achieved if duration of quartz deposition is longer than the time required for isotope exchange to occur between quartz and the hydrothermal fluid (Cole et al., 1992). Oxygen isotope exchange between quartz and the hydrothermal fluid (< 20 years at 300 °C, Cole et al., 1992) is one to several orders of magnitude faster than estimated quartz growth rate in hydrothermal systems (e.g., Walderhaug, 1994; Mercer et al., 2015; Pollington et al., 2016; Cernuschi et al., 2018; Li et al., 2018). However, disequilibrium partitioning of oxygen isotopes in quartz can possibly occur as a result of different growth rates between the crystallographic faces of a same crystal (e.g., sector zoning; Onasch and Vennemann, 1995; Tanner et al., 2013) or during fast growth rate periods (Onasch and Vennemann, 1995; Allan and Yardley, 2007). Influence of sector zoning on the $\delta^{18}O_{quartz}$ value is not well defined and seems to be either null or low (< 2‰ Klemm et al., 1990 and 1991; Onasch and Vennemann, 1995; Jourdan et al., 2009a; Tanner et al., 2013). Quartz precipitating during fast growth rate periods are characterized by more structural defects, and thus, by higher concentration of trace elements (Ihinger and Zink, 2000; Götte et al., 2011). In the studied quartz crystal, the important $\delta^{18}O_{quartz}$ variations are not linked to specific SEM-CL textures or trace element content suggesting that they are not linked to fast growth rate periods. Therefore, in the following discussion isotopic equilibrium is assumed between quartz and fluid and the calculated $\delta^{18}O_{fluid}$ values should be considered as minimum. Possible post-crystallization modification of $\delta^{18}O_{quartz}$ by diffusion can be discarded, as diffusive exchange of oxygen isotopes in quartz is inefficient at temperature lower than 300 °C, requiring more than 1 My to diffuse over <15 μm (Farver and Yund, 1991), the latter value corresponding to the spot size of in-situ oxygen isotope measurement by SIMS (i.e., 15 μm).

5.2.2. Origin and mixing history of the mineralizing fluids

5.2.2.1. Origin of the mineralizing fluids of stages A, B_1 and B_2. As discussed by Rottier et al. (2018a), mineralization stages A, B_1, and B_2 are thought to be formed by mixing at shallow levels of rising magmatic moderate-salinity metal-rich fluids (~20 wt% NaCl equiv.) with a surface-derived low-salinity fluid (< 2.5 wt% NaCl equiv.) stored below the paleowater table. The observed range of salinities requires that the magmatic fluids have been mixed with the surface-derived fluid in a proportion up to 1:10. Fluid inclusion assemblages measured by Rottier et al. (2018a) in the same quartz crystals on which the SIMS analyses have been performed can give insights into the signature of the fluids involved in the mixing. We define the footprint of a FIA as the area enclosing the assemblage when projected onto the surface of the quartz considered (Figs. 4A, 6A, 7A, A.1 and A.2). A footprint may contain several growth bands. The $\delta^{18}O_{quartz}$ for each footprint is estimated using SIMS analyses performed on those growth bands, using a mean value when several analyses are available. Important assumptions in this approach are that the $\delta^{18}O_{quartz}$ for a given footprint is representative of that of the quartz precipitated during fluid entrapment and that $\delta^{18}O_{quartz}$ is similar along the same growth band. The calculated $\delta^{18}O_{fluid}$ and the average salinity of the fluid inclusion assemblages show a rough positive correlation (Fig. 9). The calculated oxygen isotope composition of the fluid corresponding to FIAs having the lowest (2.7 wt%) and the highest (18.3 wt%) salinity is 4.2‰ and 9.8‰, respectively. The obtained composition of the moderate-salinity metal-rich magmatic fluid, 9.8‰, is coherent with the fact that only 6 over 141 calculated $\delta^{18}O$ values of fluids in equilibrium with quartz crystals from stages A, B_1 and B_2, have a slightly heavier $\delta^{18}O$ signature with a maximum at 10.9‰ (Fig. 2). The obtained $\delta^{18}O_{H2O}$ is also in agreement with the calculated $\delta^{18}O$ values of the magmatic fluids in equilibrium with quartz from the porphyry-type mineralization found at Cerro de Pasco, ranging between 8.5 and 9.6‰ for quartz from the quartz-magnetite-chalcopyrite-(pyrite) porphyry-style veinlets crosscutting the small porphyritic trachyte intrusions (PM2; Fig. 2; Rottier et al., 2016b) and between 10.6 and 11.6‰ for quartz from quartz-molybdenite-(chalcopyrite)-(pyrite) veins found in clasts from the diatreme-breccia (PM1; Figs. 1a and 2; Rottier et al.,

Table 4
Comparison of temperatures (°C) obtained with various Ti-in-quartz thermobarometers and those obtained by fluid inclusion microthermometry from Rottier et al. (2018a).

Stage	Sample	Ti content (ppm)		Thomas et al. (2010)		Huang and Audétat (2012)		Zhang et al. (2020)		Fluid inclusions	
		min	*max*	*min*	*max*	*min*	*max*	*min*	*max*	*min*	*max*
A	BR-111	1,9	2,1	285	290	276	280	197	201	249 ± 7	261 ± 7
B_1	BR-05 Q1	1,6	10	278	366	268	361	190	275	248 ± 4	280 ± 4
B_1	BR-12-Q2	1,1	6,5	263	343	253	336	176	253	240 ± 9	
B_1	BR-12-Q5	0,9	6,6	255	344	244	337	169	254	(358 ± 11)[a]	
B_1	CV-11 Q6	1,1	7,5	263	351	253	344	176	260	209 ± 7	261 ± 2
B_2	BR-126 Q6	1,7	3,2	281	309	271	300	193	219	250 ± 4	
B_2	CV-11 Q7	1	5,9	259	338	249	331	173	248	264 ± 5	
C_1	Br-24-Q1	3,5	4,9	313	328	304	321	223	239	294 ± 1	

[a] Secondary fluid inclusions not representative of quartz precipitation temperature.

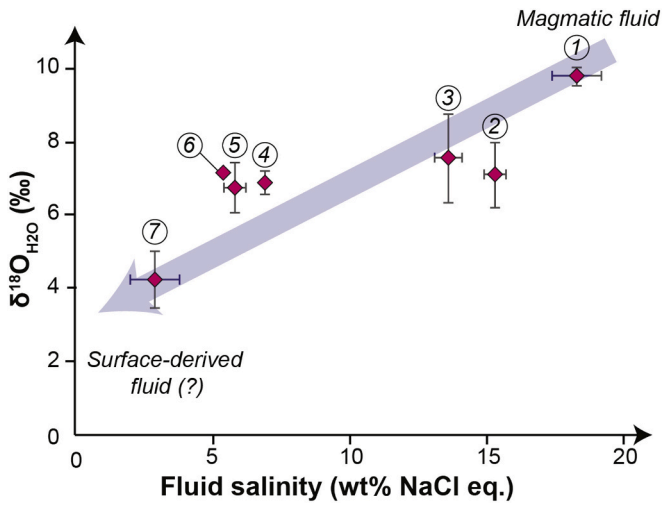

Fig. 9. Correlation between fluid inclusion salinity from FIAs hosted in quartz and calculated $\delta^{18}O$ values of the fluids. Error bars for salinity correspond to the 1 sigma variation inside each FIA, and the ones for the $\delta^{18}O_{H2O}$ values correspond to the range of values considering the 1 sigma variation of the homogenization temperatures inside each FIA. (1) sample BR-05-Q1 – stage B1; (2) sample BR-175– stage A; (3) sample BR-175– stage A; (4) sample CV-11-Q7 – stage B2; (5) sample BR-111 – stage A; (6) sample BR-126 – stage B2; (7) sample CV-11-Q6 – stage B2.

2018b). Thus, a value of 10‰ appears to be a good estimation of the oxygen isotope composition of the rising moderate-salinity metal-rich magmatic fluid. The calculated $\delta^{18}O_{H2O}$ of 4‰ for the fluid having the lowest salinity (2.7 wt% NaCl equiv.) is probably higher than the true $\delta^{18}O$ composition of the surface-derived low-salinity fluid, as it can already be a mixing product of the two fluids. Therefore, the surface-derived fluid end-member probably has a $\delta^{18}O_{H2O} < 4‰$. In addition, a composition $\delta^{18}O_{H2O} < 0‰$ for this fluid is unlikely as almost all calculated $\delta^{18}O_{H2O}$ from the obtained $\delta^{18}O_{quartz}$ are between 0‰ and 10‰ (Fig. 2) and considering that the magmatic moderate-salinity fluids need to be diluted with 90% of the surface-derived low-salinity fluid. The $\delta^{18}O_{H2O}$ for the surface-derived fluid can be estimated graphically on Fig. 9 between 0 and 4‰. This estimated $\delta^{18}O_{H2O}$ is too heavy to be a pure paleo-meteoric water (− 13 ± 1‰, Baumgartner et al., 2008). Such range can be either explained by isotopic exchange between meteoric water and the surrounding rocks and/or by the fact that the surface-derived fluid is not a pure paleo-meteoric water. To evaluate the first possibility, the isotopic exchange between the paleo-meteoric water and the main lithologies (magmatic rocks; Excelsior phyllites; Pucará limestone) present in the district has been modeled. Details on the equation and on the mineralogy and isotopic signatures of the different lithologies used for the model are described in supplementary file A.1. The results of the modeling for different water/rock ratios and temperatures are shown in Figs. 10A to 10C. The model suggests that re-equilibrated meteoric water would reach an oxygen isotope composition of >0‰ only at low water-rock ratio. At 250 °C, the required water/rock ratio is ~0.6 for Pucará limestone, of ~0.5 for Excelsior phyllites, and of ~0.4 for the diatreme breccia. Such low water/rock ratio would imply that an important volume of the mineral present in the rocks has been replaced by hydrothermal minerals, which is unlikely, considering the weak reactivity of meteoric water with respect to rock alteration (Giggenbach, 1993). By inference, it is likely that the surficial low-salinity fluid was not a pure meteoric water. At Cerro de Pasco, the temperature between ~200° and ~280 °C of the surface-derived low-salinity fluid suggests that the shallow hydrothermal system was strongly influenced by the magmatic activity and this low-salinity fluid was probably similar to the chloride waters found in many active geothermal systems (Giggenbach, 1992; Simmons et al., 2016). In such environments, discharge of magmatic vapors into the aquifer is a common process (e.g., Giggenbach, 1992) and is often invoked to explain the high $\delta^{18}O_{H2O}$ (up to 6‰) signature found in aquifers from many active volcanic fields such as the Ngawha Field (New Zealand, Simmons et al., 2016), the Osorezan and Esan fields (Japan, Giggenbach, 1992), the Vulcano Island Field (Italy, Federico et al., 2010), and the ones of the Azores archipelago (Cruz and França, 2006). At Cerro de Pasco, the large volume of rocks affected by argillic and advanced argillic alteration cropping out in the northern and southern part of the district (Fig. 1B) is indicative of such a vapor discharge, as these alteration styles are interpreted to be formed by interaction of condensed magmatic vapor with the meteoric water aquifer (Sillitoe and Hedenquist, 2003 and references therein). However, the exact quantity of condensed magmatic vapor in the aquifer cannot be estimated precisely due to the likely isotopic re-equilibration of the fluid with the country rocks during alteration. Considering a case where 30 mass. % of condensed magmatic vapors with a $\delta^{18}O_{H2O}$ of 10‰ is introduced into an aquifer dominated by meteoric water ($\delta^{18}O_{H2O} = -13‰$), the isotopic composition of the resulting fluids would be close to −6‰. The fluid resulting from such mixing would be more reactive, facilitating water-rock isotopic exchange. Isotopic re-equilibration to a $\delta^{18}O_{H2O}$ of >0‰ of such mixed fluid ($\delta^{18}O_{H2O} = -6‰$) with the surrounding rocks would require a water/rock ratio of ~1.2 for the Pucará limestone, of ~0.8 for the Excelsior phyllite, and of ~0.5 for the diatreme breccia (at 250 °C; Fig. 10D-F). Such water/rock ratios are not unrealistic considering the large alteration zone observed in the diatreme breccia and the important silicification affecting the Pucará limestone surrounding the mineralization (Rottier et al., 2018a), in addition similar water/rock ratios have been suggested for re-equilibrated meteoric water in several Au-Ag epithermal deposits (e.g., O'Neil and Silberman, 1974; Richards and Kerrich, 1993; Faure et al., 2002).

5.2.2.2. Conditions of fluid mixing during mineralization stages A, B_1 and B_2. Mixing in different proportions between the surface-derived low-salinity and the moderate-salinity metal-rich fluids having oxygen isotope compositions of ~0‰ and of ~10‰, respectively, could explain most variations of the $\delta^{18}O_{quartz}$ from stages A, B_1, and B_2 (Fig. 11 A and B). The observed $\delta^{18}O_{quartz}$ variations inside the different growth bands of the quartz crystals indicate that mixing between the two identified fluids was not a continuous process. The different studied quartz crystals recorded different histories of fluid mixing, and no isotopic signature pattern specific to each mineralization stage has been observed. Quartz crystals CV-11 Q6 and CV-11 Q7 from stage B_2 show progressive $\delta^{18}O_{quartz}$ increase and/or decrease during crystal growth, suggesting that they crystallized during episodes where the two end-member fluids were progressively mixed in different proportions. However, large part of quartz grains BR-111 (stage A), BR-12 Q2 (stage B_1), and BR-126 (stage B_2) have roughly homogeneous $\delta^{18}O$ composition, showing that they mainly crystallized from fluids having been mixed in constant proportions. In all quartz crystals, sharp changes of $\delta^{18}O_{quartz}$ are observed suggesting that during the quartz precipitation transient episodes with important variation in the proportion of the involved fluids occurred. Three low $\delta^{18}O_{quartz}$ values (< 7‰) were observed in sample BR-12 Q2, the calculated isotopic composition of the fluid in equilibrium with these parts of the quartz is <0‰, i.e., lower than the estimated oxygen isotope composition of the surface-derived low-salinity fluid. These low $\delta^{18}O_{quartz}$ values are difficult to explain only by changes in the proportion of the mixing fluids or by temperature variations and they rather can be interpreted as transient meteoric water recharge into the aquifer (Fig. 11B). For instance, the sharp $\delta^{18}O_{quartz}$ drop from 15‰ to 4.6‰ in less than 100 μm observed in the middle of quartz crystal BR-12 Q2 (stage B_1) can be the record of such meteoric water recharge into the aquifer.

All these observations suggest that fluid mixing during mineralization stages A, B_1 and B_2 was not a continuous process and that these

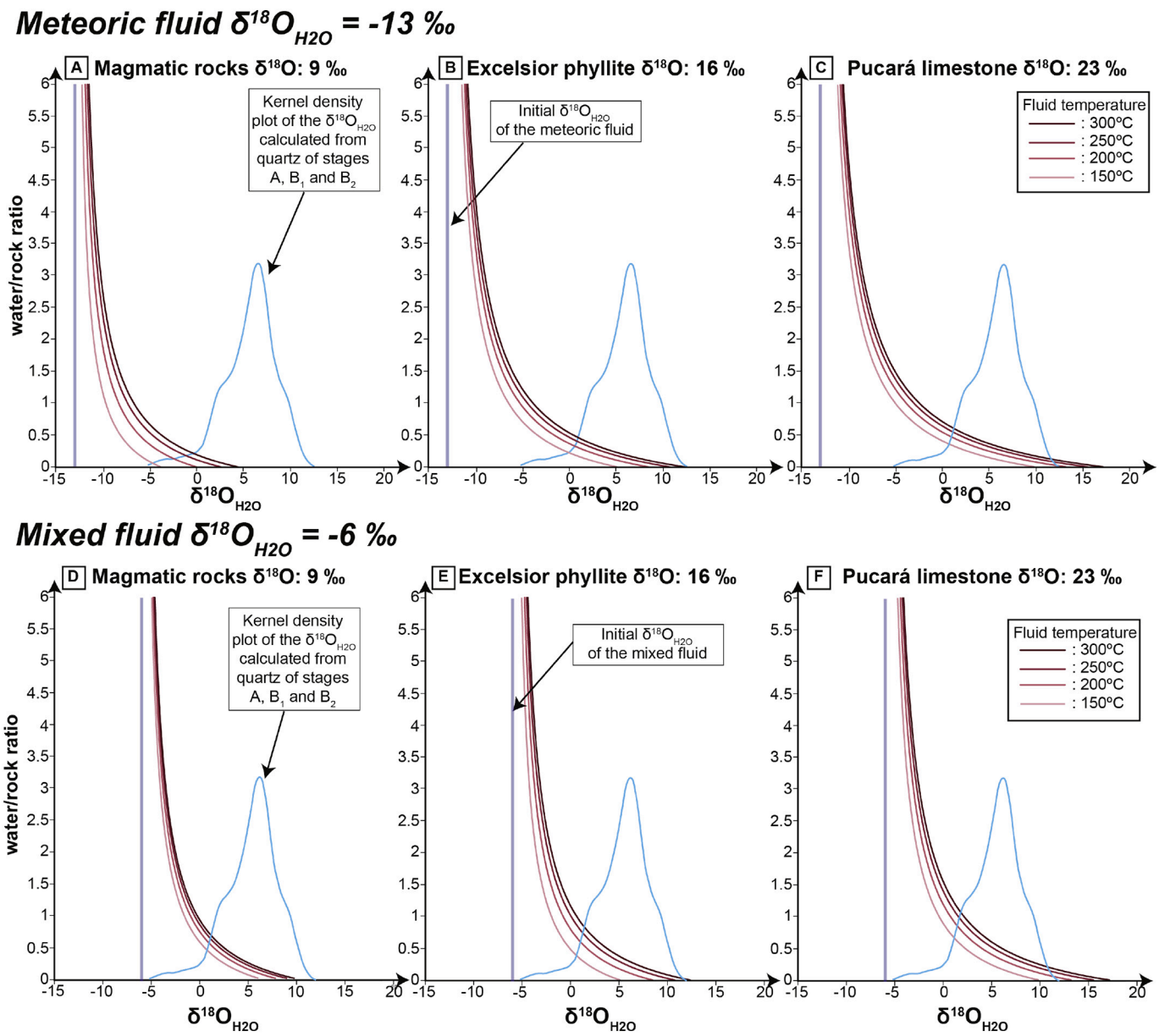

Fig. 10. Meteoric water (A, B and C) and mixed meteoric water with 30% of magmatic vapors (D, E, and F) isotopic composition after isotopic exchange with different host rock as function of water-rock ratios and different equilibration temperatures (look to Supplementary file A.1 for the details).

mineralization stages were formed by multiple, volumetric inputs of moderate-salinity metal-rich fluid into an aquifer dominated by surface-derived low-salinity fluid, possibly punctually recharged by fresh meteoric waters. Dilution of the moderate-salinity metal-rich fluid is interpreted as the main process triggering sulfide precipitation during the mineralization stages in the upper portions of the hydrothermal system (Rottier et al., 2018a). In all samples from these mineralization stages, sulfide and quartz precipitation appears to be synchronous and no petrographic indicators allow to link sulfide precipitation events to specific growth bands of the quartz crystals. This suggests that sulfide precipitation was relatively continuous during the growth of the different quartz grains. However, it is likely that the quantity of sulfides having precipitated during these stages also varied in an episodic way as function of the relative proportion of the mixed fluids. The observed strongly variable isotopic signatures of the mineralizing fluids can partly explain the large variation in trace elements content reported in sphalerite and pyrite from these stages (Rottier et al., 2018a).

5.2.2.3. Origin of the mineralizing fluids during stage C_2. Quartz-enargite veins of stage C_2 are interpreted to be formed by the ascent of CO_2-bearing contracted vapors, probably partly mixed with surface-derived low-salinity fluid (Rottier et al., 2018a). Salinity of the fluid forming quartz-enargite veins of stage C_2, between 1.2 and 2.7 wt% NaCl equiv. (Rottier et al., 2018a) is significantly lower than for stages A, B_1, and B_2. For the quartz-enargite veins of stage C_2, variation of $\delta^{18}O_{quartz}$ can be only discussed for quartz crystal BR-24 Q1 (Fig. 8A). In contrast to quartz from the other stages (A, B_1, and B_2), in quartz crystal BR-24 Q1 there is a clear correlation between $\delta^{18}O_{quartz}$, trace element content, and SEM-CL intensity and textures (Figs. 8A-C). The core and the cracks are characterized by low $\delta^{18}O_{quartz}$ values (between 7.6 and 10.4‰), by low and quite homogeneous SEM-CL intensity, and by low Al content (Figs. 8A-C). No fluid inclusions hosted in the core and the cracks have been found by Rottier et al. (2018a), thus the oxygen isotope signature of the fluid forming this dark core and the cracks cannot be calculated. However, the low $\delta^{18}O_{quartz}$ and low trace element contents of these parts suggest that they have precipitated from a surface-derived low-

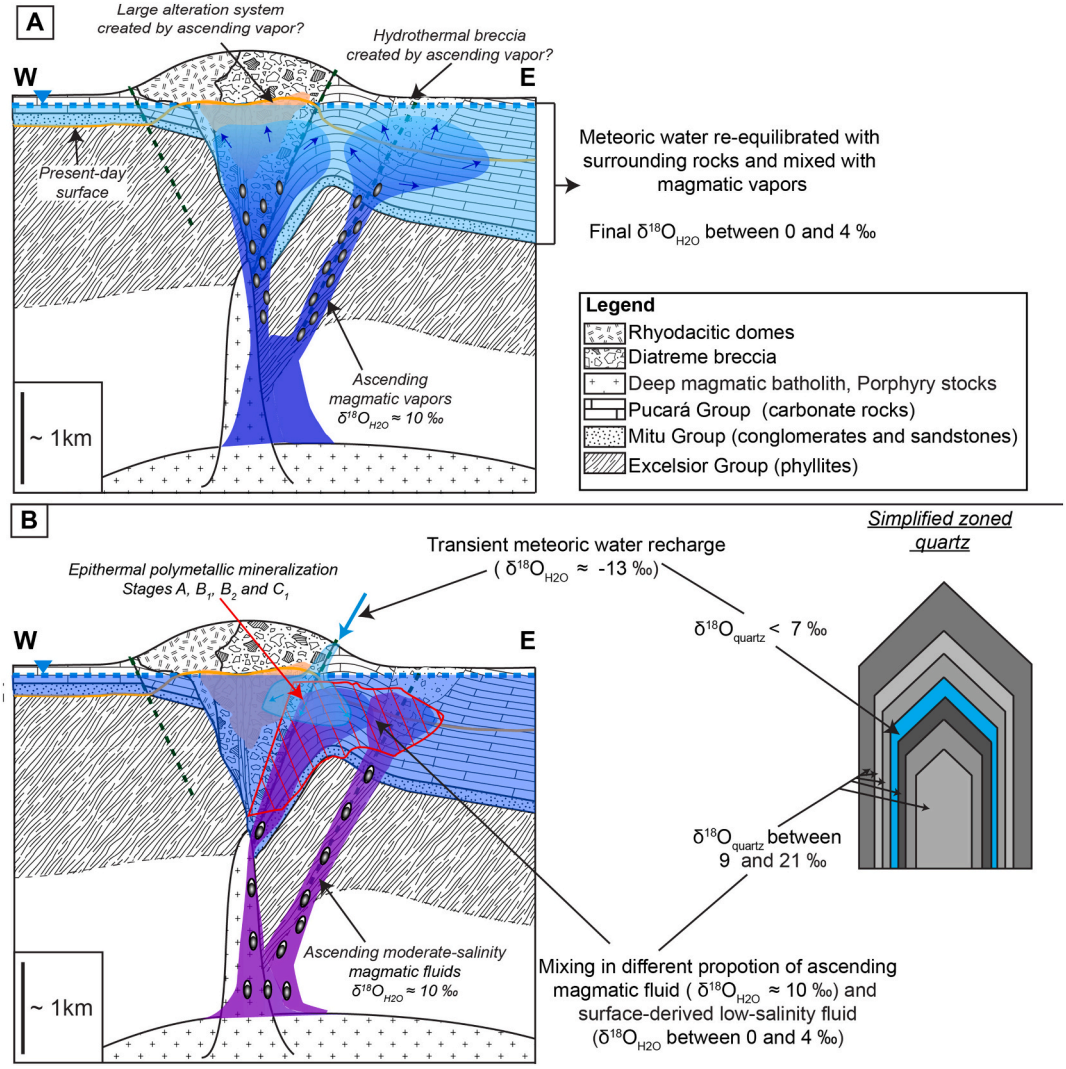

Fig. 11. Simplified ketch of the fluid mixing processes at the origin of mineralization stage A, B_1 and B_2. A) Generation of the surface-derived low-salinity fluid by mixing between meteoric water and magmatic vapors and re-equilibration with the surrounding rocks. B) Mixing between rising moderate-salinity magmatic fluid and a surfaced-derived low-salinity fluid, and local meteoric water recharge in the aquifer. Mechanisms at the origin of the moderate-salinity magmatic fluid are detailed in Rottier et al. (2018a).

salinity–dominated fluid. The quartz overgrowth in sample BR-24 Q1 is characterized by higher $\delta^{18}O_{quartz}$ values, between 13.2 and 18.6‰, high SEM-CL intensity, showing fine oscillatory zoning, and higher trace element contents (Figs. 8A-C) than the core and the cracks. This overgrowth is interpreted to be formed mainly by CO_2-bearing contracted vapor between 260° and 280 °C, the calculated $\delta^{18}O$ composition of the fluid using an average temperature of 270 °C is between 5.1 and 10.3‰. The highest value is compatible with the oxygen isotope signature of the magmatic fluid endmember at Cerro de Pasco (~10‰) and the lowest value can be explained with up to 50% of mixing with the low-salinity fluids (~ 0‰). This proportion of mixed fluids also explains the observed decrease of salinity from 2.7 to 1.2 wt% NaCl equiv., recorded by the fluid inclusion assemblages studied by Rottier et al. (2018a). In quartz-enargite veins of stage C_2, enargite precipitated after quartz and hosts fluid inclusions characterized by lower temperature (200° to 230 °C) but having similar salinity to those hosted in the quartz rims. The similar salinity suggests that enargite has precipitated from a similar fluid than the one forming the quartz overgrowth, but that enargite has probably precipitated in response to cooling of this fluid.

6. Conclusions

The oxygen isotope and trace element studies performed along growth bands of selected quartz crystals reveal the complexity of the hydrothermal processes occurring during the different mineralization stages of the Cerro de Pasco deposit. Trace element content of the epithermal quartz is extremely variable for all mineralization stages. Despite that, the chemical and physical parameters of the mineralizing fluids have been well constrained by this study and previous ones, the quartz trace element concentration variations cannot be ascribed to one specific chemical or physical parameter such as temperature, pressure, fO_2, quartz growth rate, or fluid composition.

The significant variations, up to 11.5‰, of the $\delta^{18}O_{quartz}$ value in a single crystal observed at Cerro de Pasco confirm the effectiveness of in-situ analysis with regards to bulk isotope analysis to reconstruct the origin of mineralizing fluids of epithermal ore deposits. At Cerro de Pasco, the important variations in $\delta^{18}O_{quartz}$ compositions are not ascribed to fluctuation of precipitation temperatures and are rather explained by mixing at the site of mineralization, in different proportions, of a rising moderate-salinity magmatic fluid and a surfaced-derived low-salinity fluid with a $\delta^{18}O_{fluid}$ signature of ~10‰ and between 0 and 4‰, respectively. The low-salinity fluid is interpreted to be

generated by mixing between meteoric water and magmatic vapors, and that it has been re-equilibrated with the surrounding rocks. During mineralization stages A, B_1 and B_2 the proportions of the two fluids (moderate-salinity and low-salinity) were strongly variable. It suggests that mineralization stages A, B_1, and B_2 were formed by multiple transient pulses of a rising moderate-salinity magmatic fluid into an aquifer dominated by the low-salinity fluid. These pulses of magmatic fluid were the source of base metals and their dilution triggered sulfide precipitation during these hydrothermal events. In addition, sharp $\delta^{18}O_{quartz}$ drops identified by SIMS in-situ oxygen isotope analyses are likely to record transient meteoric water recharge into the aquifer. Quartz overgrowth of stage C_2 are compatible with that mineralizing fluid forming the diatreme-hosted enargite-pyrite veins resulted from a mixing of rising CO_2-bearing contracted vapors with less than 50% of the surficial low-salinity fluid.

In this study, even quartz grains from the same mineralization stage show different and variable $\delta^{18}O_{quartz}$ compositions that are interpreted as resulting from mixing in variable proportions of the two fluids (moderate-salinity and low-salinity). A conclusion of this study is that tracing the mineralizing fluids forming epithermal deposits in the shallow part of a porphyry system requires high spatial resolution in-situ oxygen isotope analyses of multiple quartz grains from the same mineralization stage to obtain a clearer picture of the fluids origin and mixing processes.

Declaration of Competing Interest

None.

Acknowledgements

This study was supported by the Swiss National Science Foundation (project FN 200020_134872). Funding for the SwissSIMS facility was provided by the KIP 6 “CASA” to LPB. We thank Volcan Compañía Minera S.A. for providing financial and logistical support. Special thanks to the Cerro de Pasco and Volcan Geology staff, in particular to Hugo Alvarez, David Cuellar, César Farfán and Ronner Bendezú. We gratefully acknowledge Jean-Marie Boccard and Fabio Capponi for their help with sample preparation. We are grateful to Antonin Richard and Phillipe Boulvais for their constructive comments.

Appendix A. Supplementary data

Supplementary data to this article can be found online at https://doi.org/10.1016/j.chemgeo.2021.120277.

References

Allan, M., Yardley, B., 2007. Tracking meteoric infiltration into a magmatic-hydrothermal system: a cathodoluminescence, oxygen isotope and trace element study of quartz from Mt. Leyshon, Australia. Chem. Geol. 240, 343–360.

Angeles, C., 1999. Los sedimentos Cenozoicos de Cerro de Pasco: Estratigrafia, sedimentación y tectónica, in Machare, J., Benavides-Caceres, V., and Rosas, S., eds. Soc. Geol. del Perú 5, 103–118.

Arribas, A., 1995. Characteristics of high-sulfidation epithermal deposits, and their relation to magmatic fluid. In: Thompson, J.F.H. (Ed.), Magmas, Fluids, and Ore Deposits. Mineralogical Association of Canada, Victoria, British Columbia, pp. 419–454.

Audétat, A., Garbe-Schönberg, D., Kronz, A., Pettke, T., Rusk, B., Donovan, J.J., Lowers, H.A., 2015. Characterisation of a natural quartz crystal as a reference material for microanalytical determination of Ti, Al, Li, Fe, Mn, Ga and Ge. Geostand. Geoanal. Res. 39, 171–184.

Baumgartner R (2007) Sources and evolution in space and time of hydrothermal fluids at the Cerro de Pasco Cordilleran base metal deposit, Central Peru Terre & Environnement 66. https://doi.org/10.13097/archiveouverte/unige:98205.

Baumgartner, R., Fontboté, L., Vennemann, T., 2008. Mineral zoning and geochemistry of epithermal polymetallic Zn-Pb-Ag-Cu-Bi mineralization at Cerro de Pasco. Peru. Econ. Geol. 103, 493–537.

Baumgartner, R., Fontboté, L., Spikings, R., Ovtcharova, M., Schneider, J., Pace, L., Gutjahr, M., 2009. Bracketing the age of magmatic-hydrothermal activity at the Cerro de Pasco epithermal polymetallic deposit, Central Peru: a U-Pb and 40Ar/39Ar study. Econ. Geol. 104, 479–504.

Bendezú, R., Fontboté, L., 2009. Cordilleran epithermal Cu-Zn-Pb-(Au-Ag) mineralization in the Colquijirca District, Central Peru: deposit-scale mineralogical patterns. Econ. Geol. 104, 905–944.

Beuchat, S., Moritz, R., Pettke, T., 2004. Fluid evolution in the W-Cu-Zn-Pb San Cristobal vein, Peru: Fluid inclusion and stable isotope evidence. Chem. Geol. 210, 201–224.

Bissig, T., Tosdal, R.M., 2009. Petrogenetic and metallogenetic relationships in the Eastern Cordillera Occidental of Central Peru. J. Geol. 117, 499–518.

Bissig, T., Ullrich, T.D., Tosdal, R.M., Friedman, R., Ebert, S., 2008. The time-space distribution of Eocene to Miocene magmatism in the central Peruvian polymetallic province and its metallogenetic implications. J. S. Am. Earth Sci. 26, 16–35.

Bussell, M.A., Alpers, C.N., Petersen, U., Shepherd, T.J., Bermudez, C., Baxter, A.N., 1990. The Ag-Mn-Pb-Zn vein, replacement, and skarn deposits of Uchucchacua, Peru; studies of structure, mineralogy, metal zoning, Sr isotopes, and fluid inclusions. Econ. Geol. 85, 1348–1383.

Catchpole, H., Kouzmanov, K., Putlitz, B., Seo, J., Fontboté, L., 2015. Zoned base metal mineralization in a porphyry system: origin and evolution of mineralizing fluids in the Morococha district. Peru. Econ. Geol. 110, 39–71.

Cernuschi, F., Dilles, J.H., Grocke, S.B., Valley, J.W., Kitajima, K., Tepley, F.J., 2018. Rapid formation of porphyry copper deposits evidenced by diffusion of oxygen and titanium in quartz. Geology 46, 611–614.

Clayton, R.N., Mayeda, T.K., 2009. Kinetic isotope effects in oxygen in the laboratory dehydration of magnesian minerals. J. Phys. Chem. A 113, 2212–2217.

Cole, D.R., Ohmoto, H., Jacobs, G.K., 1992. Isotopic exchange in mineral-fluid systems: III. Rates and mechanisms of oxygen isotope exchange in the system granite-H2O±NaCl±KCl at hydrothermal conditions. Geochim. Cosmochim. Acta 56, 445–466.

Cruz, J.V., França, Z., 2006. Hydrogeochemistry of thermal and mineral water springs of the Azores archipelago (Portugal). J. Volcanol. Geotherm. Res. 151, 382–398.

Deen, J.A., Rye, R.O., Munoz, J.L., Drexler, J.W., 1994. The magmatic hydrothermal system at Julcani, Peru; evidence from fluid inclusions and hydrogen and oxygen isotopes. Econ. Geol. 89, 1924–1938.

Dilles, J.H., 1987. Petrology of the Yerington Batholith, Nevada; evidence for evolution of porphyry copper ore fluids. Econ. Geol. 82, 1750–1789.

Eastoe, C.J., 1978. A fluid inclusion study of the Panguna porphyry copper deposit, Bougainville, Papua New Guinea. Econ. Geol. 73, 721–748.

Einaudi, M.T., 1968. Pyrrhotite-Pyrite-Sphalerite Relations at Cerro de Pasco, Peru. Unpublished Ph.D. thesis. Harvard University, Cambridge, MA, p. 381.

Einaudi, M.T., 1977. Environment of ore deposition at Cerro de Pasco. Peru. Econ. Geol. 72, 893–924.

Farver, J.R., Yund, R.A., 1991. Oxygen diffusion in quartz: dependence on temperature and water fugacity. Chem. Geol. 90, 55–70.

Faure, K., Matsuhisa, Y., Metsugi, H., Mizota, C., Hayashi, S., 2002. The Hishikari Au-Ag epithermal deposit, Japan: oxygen and hydrogen isotope evidence in determining the source of paleohydrothermal fluids. Econ. Geol. 97, 481–498.

Federico, C., Capasso, G., Paonita, A., Favara, R., 2010. Effects of steam-heating processes on a stratified volcanic aquifer: stable isotopes and dissolved gases in thermal waters of Vulcano Island (Aeolian archipelago). J. Volcanol. Geotherm. Res. 192, 178–190.

Field, C.W., Zhang, L., Dilles, J.H., Rye, R.O., Reed, M.H., 2005. Sulfur and oxygen isotopic record in sulfate and sulfide minerals of early, deep, pre-Main Stage porphyry Cu–Mo and late Main Stage base-metal mineral deposits, Butte district, Montana. Chem. Geol. 215 (1–4), 61–93.

Flem, B., Müller, A., 2012. In situ analysis of trace elements in quartz using laser ablation inductively coupled plasma mass spectrometry. In: Quartz: Deposits, Mineralogy and Analytics. Springer, Berlin, Heidelberg, pp. 219–236. https://doi.org/10.1007/978-3-642-22161-3_10.

Giggenbach, W.F., 1992. Isotopic shifts in waters from geothermal and volcanic systems along convergent plate boundaries and their origin. Earth Planet. Sci. Lett. 113, 495–510.

Giggenbach, W.F., 1993. Reply to comment by P. Blattner: “Andesitic water”: a phantom of the isotopic evolution of water-silicate systems. E&PSL 120 (3–4), 519–522.

Götte, T., Pettke, T., Ramseyer, K., Koch-Müller, M., Mullis, J., 2011. Cathodoluminescence properties and trace element signature of hydrothermal quartz: a fingerprint of growth dynamics. Am. Mineral. 96, 802–813.

Guillong, M., Heinrich, C.A., 2007. LA-ICP-MS Analysis of Inclusions: Improved Ablation and Detection: European Current Research on Fluid Inclusions (ECROFI-XIX), at Bern, p. 82.

Guillong, M., Meier, D.L., Allan, M.M., Heinrich, C.A., Yardley, B.W.D., 2008. SILLS: A Matlab-based program for the reduction of Laser Ablation ICP-MS data of homogeneous materials and inclusions. In: Sylvester, P. (Ed.), Laser-Ablation-ICPMS in the Earth Sciences: Current Practices and Outstanding Issues. Mineralogical Association of Canada, Vancouver, BC, pp. 328–333.

Günther, D., Frischknecht, R., Heinrich, C.A., Kahlert, H.J., 1997. Capabilities of an Argon Fluoride 193 nm excimer laser for laser ablation inductively coupled plasma mass spectrometry microanalysis of geological materials. J. Anal. At. Spectrom. 12, 939–944.

Günther, D., Audétat, A., Frischknecht, R., Heinrich, C.A., 1998. Quantitative analysis of major, minor and trace elements in fluid inclusions using laser ablation–inductively coupled plasmamass spectrometry: J. Anal. At. Spectrom. 13, 263–270.

Hedenquist, J.W., Lowenstern, J.B., 1994. The role of magmas in the formation of hydrothermal ore deposits. Nature 370, 519.

Heinrich, C.A., Pettke, T., Halter, W.E., Aigner-Torres, M., Audétat, A., Günther, D., Hattendorf, B., Bleiner, D., Guillong, M., Horn, I. (2003) Quantitative multi-element

analysis of minerals, fluid and melt inclusions by laser-ablation inductively-coupled-plasma mass-spectrometry: Geochim. Cosmochim. Acta 67, 3473–3496.
Henley, R.W., McNabb, A., 1978. Magmatic vapor plumes and ground-water interaction in porphyry copper emplacement. Econ. Geol. 73, 1–20.
Huang, R., Audétat, A., 2012. The titanium-in-quartz (TitaniQ) thermobarometer: a critical examination and re-calibration: Geochim. Cosmochim. Acta 84, 75–89.
Ihinger, P.D., Zink, S.I., 2000. Determination of relative growth rates of natural quartz crystals. Nature 404, 865–869.
Jourdan, A.L., Vennemann, T.W., Mullis, J., Ramseyer, K., 2009a. Oxygen isotope sector zoning in natural hydrothermal quartz. Min. Mag. 73, 615–632.
Jourdan, A.L., Vennemann, T.W., Mullis, J., Ramseyer, K., Spiers, C.J., 2009b. Evidence of growth and sector zoning in hydrothermal quartz from Alpine veins. Eur. J. Mineral. 21, 219–231.
Klemm, A., Banerjee, A., Hoernes, S., 1990. A new intracrystalline isotope effect: 18O under the faces of amethyst. Z. Naturforsch. A 45, 1374–1376.
Klemm, A., Banerjee, A., Hoernes, S., 1991. Fractionation of oxygen isotopes at the faces of smoky quartz. Z. Naturforsch. A 46, 1133–1134.
Landtwing, M.R., Pettke, T., 2005. Relationships between SEM-cathodoluminescence response and trace-element composition of hydrothermal vein quartz. Am. Mineral. 90, 122–131.
Lehmann, K., Pettke, T., Ramseyer, K., 2011. Significance of trace elements in syntaxial quartz cement, Haushi Group sandstones, Sultanate of Oman. Chem. Geol. 280 (1–2), 47–57.
Li, Y., Li, X.H., Selby, D., Li, J.W., 2018. Pulsed magmatic fluid release for the formation of porphyry deposits: Tracing fluid evolution in absolute time from the Tibetan Qulong Cu-Mo deposit. Geology 46, 7–10.
Mercer, C.N., Reed, M.H., Mercer, C.M., 2015. Time scales of porphyry Cu deposit formation: Insights from titanium diffusion in quartz. Econ. Geol. 110, 587–602.
Noble, D.C., McKee, E.H., 1999. The Miocene metallogenic belt of central and northern Peru. In: Skinner, B.J. (Ed.), Geology and Ore Deposits of the central Andes, 7. Society of Economic Geology Special Publication, pp. 155–193.
Norman, D.I., Landis, G.P., 1983. Source of mineralising components in hydrothermal ore fluid as evidenced by $^{87}Sr/^{86}Sr$ and stable isotope data from the Pasta Bueno deposit. Peru. Econ. Geol. 78, 451–465.
Onasch, C.M., Vennemann, T.W., 1995. Disequilibrium partitioning of oxygen isotopes associated with sector zoning in quartz. Geology 23, 1103–1106.
O'Neil, J.R., Silberman, M.L., 1974. Stable isotope relations in epithermal Au-Ag deposits. Econ. Geol. 69, 902–909.
Pettke, T., Oberli, F., Audétat, A., Guillong, M., Simon, A.C., Hanley, J.J., Klemm, L.M., 2012. Recent developments in element concentration and isotope ratio analysis of individual fluid inclusions by laser ablation single and multiple collector ICP-MS. Ore Geol. Rev. 44, 10–38.
Pollington, A.D., Kozdon, R., Anovitz, L.M., Georg, R.B., Spicuzza, M.J., Valley, J.W., 2016. Experimental calibration of silicon and oxygen isotope fractionations between quartz and water at 250 C by in situ microanalysis of experimental products and application to zoned low $\delta^{30}Si$ quartz overgrowths. Chem. Geol. 421, 127–142.
Richards, J.P., Kerrich, R., 1993. The Porgera gold mine, Papua New Guinea; magmatic hydrothermal to epithermal evolution of an alkalic-type precious metal deposit. Econ. Geol. 88, 1017–1052.
Rogers, R., (1983). Structural and geochemical evolution of a mineralized volcanic vent at Cerro de Pasco, Peru. Unpublished PhD Thesis, University of Arizona, 116 p.
Rosas, S., Fontboté, L., Tankard, A., 2007. Tectonic evolution and paleogeography of the Mesozoic Pucará Basin, Central Peru. J. S. Am. Earth Sci. 26, 16–35.
Rottier, B., Casanova, V., 2020. Trace element composition of quartz from porphyry systems: a tracer of the mineralizing fluid evolution. Mineral. Deposita 1–20.
Rottier, B., Kouzmanov, K., Wälle, M., Bendezú, R., Fontboté, L., 2016a. Sulfide replacement processes revealed by textural an LA-ICP-MS trace element analyses: example from the early mineralization stages at Cerro de Pasco, Peru: Econ. Geol. 111, 1347–1367.
Rottier, B., Kouzmanov, K., Bouvier, A.-S., Baumgartner, L., Wälle, M., Rezeau, H., Bendezú, R., Fontboté, L., 2016b. Heterogeneous melt and hypersaline liquid inclusions in shallow porphyry type mineralization as markers of the magmatic-hydrothermal transition (Cerro de Pasco district, Peru). Chem. Geol. 447, 93–116.
Rottier, B., Kouzmanov, K., Casanova, V., Wälle, M., Fontboté, L., 2018a. Cyclic dilution of magmatic metal-rich hypersaline fluids by magmatic low-salinity fluid: a major process generating the giant epithermal polymetallic deposit of Cerro de Pasco. Peru. Econ. Geol. 113, 825–856.
Rottier, B., Kouzmanov, K., Casanova, C., Bouvier, A.-S., Baumgartner, L., Wälle, M., Fontboté, L., 2018b. Hydrothermal evolution of a hidden porphyry-type mineralization related to the large epithermal polymetallic deposit of Cerro de Pasco district (Peru): Miner. Dep. 53, 919–946.
Rottier, B., Kouzmanov, K., Ovtcharova, M., Ulianov, A., Wälle, M., Selby, D., Fontboté, L., 2020. Multiple rejuvenation episodes of a silicic magma reservoir at the origin of the large diatreme-dome complex and porphyry-type mineralization events at Cerro de Pasco (Peru). Lithos 376, 105766.
Rusk, B., 2012. Cathodoluminescent textures and trace elements in hydrothermal quartz. In: Quartz: Deposits, Mineralogy and Analytics. Springer, Berlin, Heidelberg, pp. 307–329.
Rusk, B., Koenig, A., Lowers, H., 2011. Visualizing trace element distribution in quartz using cathodoluminescence, electron microprobe, and laser ablation-inductively coupled plasma-mass spectrometry. Am. Mineral. 96, 703–708.
Rusk, B.G., Lowers, H.A., Reed, M.H., 2008. Trace elements in hydrothermal quartz: relationships to cathodoluminescence textures and insights into vein formation. Geology 36, 547–550.
Rye, R.O., Sawkins, F.J., 1974. Fluid inclusion and stable isotope studies on the Casapalca Ag-Pb-Zn-Cu deposit, Central Andes. Peru. Econ. Geol. 69, 181–205.
Saintilan, N.J., Sproson, A.D., Selby, D., Rottier, B., Casanova, V., Creaser, R.A., Kouzmanov, K., Fontboté, L., Piecha, M., Gereke, M., Zambito IV, J.J., 2021. Osmium isotopic constraints on sulphide formation in the epithermal environment of magmatic-hydrothermal mineral deposits. Chem. Geol. 120053.
Schlöglova, K., Wälle, M., Heinrich, C.A., 2017. LA-ICP-MS analysis of fluid inclusions: contamination effects challenging micro-analysis of elements close to their detection limit. J. Anal. At. Spectrom. 32, 1052–1063. https://doi.org/10.1039/C7JA00022G.
Seitz, S., Baumgartner, L.P., Bouvier, A.-S., Putlitz, B., Vennemann, T., 2017. Quartz standards for oxygen isotope and trace element analysis by SIMS. Geostand. Geoanal. Res. 41, 69–75.
Sillitoe, R.H., 1973. The tops and bottoms of porphyry copper deposits. Econ. Geol. 68, 799–815.
Sillitoe, R.H., Hedenquist, J.W., 2003. Linkages between volcanotectonic settings, ore-fluid compositions, and epithermal precious metal deposits. Spec. Publ. Soc. Econ. Geol. 10, 315–343.
Simmons, S.F., Brown, K.L., Tutolo, B.M., 2016. Hydrothermal transport of Ag, au, Cu, Pb, Te, Zn, and other metals and metalloids in New Zealand geothermal systems: Spatial patterns, fluid-mineral equilibria, and implications for epithermal mineralization. Econ. Geol. 111 (3), 589–618.
Spikings, R., Reitsma, M.J., Boekhout, F., Mišković, A., Ulianov, A., Chiaradia, M., Gerdes, A., Schaltegger, U., 2016. Characterization of Triassic rifting in Peru and implications for the early disassembly of western Pangaea. Gondwana Res. 35, 124–143.
Sun, S.S., Eadington, P.J., 1987. Oxygen isotope evidence for the mixing of magmatic and meteoric waters during tin mineralization in the Mole Granite, New South Wales, Australia. Econ. Geol. 82, 43–52.
Tanner, D., Henley, R.W., Mavrogenes, J.A., Holden, P., 2013. Combining in situ isotopic, trace element and textural analyses of quartz from four magmatic-hydrothermal ore deposits. Contrib. Mineral. Petrol. 166, 1119–1142.
Thomas, J.B., Watson, E.B., Spear, F.S., Shemella, P.T., Nayak, S.K., Lanzirotti, A., 2010. TitaniQ under pressure: the effect of pressure and temperature on the solubility of Ti in quartz. Contrib. Mineral. Petrol. 160, 743–759.
Walderhaug, O., 1994. Precipitation rates for quartz cement in sandstones determined by fluid-inclusion microthermometry and temperature-history modeling. J. Sediment. Res. 64, 324–333.
Wallier, S., Rey, R., Kouzmanov, K., Pettke, T., Heinrich, C.A., Leary, S., O'Connor, G., Tamas, C.G., Vennemann, T., Ullrich, T., 2006. Magmatic fluids in the breccia-hosted epithermal Au-Ag deposit of Rosia Montana, Romania. Econ. Geol. 101, 923–954.
Wark, D.A., Watson, E.B., 2006. TitaniQ: a titanium-in-quartz geothermometer. Contrib. Mineral. Petrol. 152, 743–754.
Zhang, C., Li, X., Almeev, R.R., Horn, I., Behrens, H., Holtz, F., 2020. Ti-in-quartz thermobarometry and TiO2 solubility in rhyolitic melts: New experiments and parametrization. Earth Planet. Sci. Lett. 538, 116213.
Zheng, Y.F., 1993. Calculation of oxygen isotope fractionation in anhydrous silicate minerals. Geochim. Cosmochim. Acta 57, 1079–1091.